Lattice thermal conductivity including phonon frequency shifts and scattering rates induced by quartic anharmonicity in cubic oxide and fluoride perovskites

Yinchang Zhao,[1,*] Shuming Zeng,[2] Geng Li,[3] Chao Lian,[4,5,†] Zhenhong Dai,[1,‡] Sheng Meng,[5,6,§] and Jun Ni[7,8]

[1]*Department of Physics, Yantai University, Yantai 264005, China*
[2]*Department of Physics, Yangzhou University, Yangzhou 225009, China*
[3]*National Supercomputer Center in Tianjin, Tianjin 300457, China*
[4]*Oden Institute and Department of Physics, The University of Texas at Austin, Austin, Texas 78712, USA*
[5]*Institute of Physics, Chinese Academy of Sciences, Beijing 100190, China*
[6]*Collaborative Innovation Center of Quantum Matter, Beijing 100871, China*
[7]*Department of Physics, Tsinghua University, Beijing 100084, China*
[8]*Frontier Science Center for Quantum Information, Beijing 100084, China*

(Received 17 September 2021; revised 15 November 2021; accepted 7 December 2021; published 15 December 2021)

Lattice thermal conductivity κ_L is one of the key parameters involved in the design of microelectronics and energy-conversion devices. In determining the κ_L, similar to the well-known cubic anharmonic effect, quartic anharmonicity is ubiquitous and also plays a crucial role in the final heat conduction of some compounds. In this paper, we use a high-throughput first-principles calculation method that combines self-consistent phonon (SCP) theory, compressive sensing techniques, and Boltzmann transport equation (BTE) to investigate the lattice thermal conductivity κ_L with the inclusion of cubic and quartic anharmonicity in 16 cubic oxide and fluoride perovskites. The BTE is solved on top of SCP theory for complete treatment of the quartic anharmonic effect that comprises four-phonon scattering and temperature-driven phonon frequency shift. In particular, only the κ_L within SCP theory is numerically valid for six of the 16 candidate perovskites, since the common calculation of BTE with harmonic phonons fails to estimate the κ_L due to the presence of imaginary frequencies in these materials. Our results exhibit that in addition to three-phonon scattering, the full inclusion of quartic anharmonicity is indispensable to capture a pertinent κ_L and rational temperature dependence of the κ_L, while the consideration of only four-phonon scatterings (phonon frequency shifts) gives rise to a lower (higher) κ_L and stronger (weaker) temperature dependence. Meanwhile, we find a roughly linear relation between the κ_L and four-phonon scatterings in the 16 perovskites, which shows that the candidates with lower κ_L have stronger four-phonon scatterings. Moreover, very strong four-phonon scatterings are discovered in some cubic perovskites, especially in fluoride perovskites with imaginary harmonic phonons. The analyses of thermal conductivity spectrum $\kappa_L(\omega)$, scattering process, phase space, etc. reveal that the low-frequency four-phonon scattering rates in the structures with low κ_L, e.g., <1 W/mK, are comparable to or even exceed those of three-phonon processes.

DOI: 10.1103/PhysRevB.104.224304

I. INTRODUCTION

Thermal conductivity of a material, an indicator of its performance to conduct heat under a finite-temperature gradient, is of vital significance in a variety of modern technologies such as photovoltaics, transistors, and thermoelectric devices [1,2]. Specially, the minimized heat transport is required in thermoelectric applications for achieving optimal energy conversion efficiency [3], while high thermal conductivity is necessary to dissipate heat in microprocessors [4]. Therefore, for semiconductors, the one exhibiting extreme lattice heat conduction, e.g., with either very low or very high lattice thermal conductivity κ_L, is of particular interest. Furthermore, with the dramatic increase in attention to admirable thermoelectrics, the materials with very low κ_L have been investigated to a large extent in past years [5–14]. At the same time, heat conduction in perovskite-type materials was also studied extensively for latent thermoelectric applications [15–22], which elucidates the importance of systematic research on the κ_L in various perovskites, e.g., the cubic oxide and fluoride perovskites to focus on in this paper.

For perovskites, there are usually rich phase diagrams, which is determined by the fact that many perovskite configurations are generated from the distortions of the ideal cubic lattice. Such a phenomenon is common in a great many perovskites [23–27]. Moreover, some perovskite structures are unstable at lower temperatures. This signifies that the traditional solution of Boltzmann transport equation (BTE) on the basis of phonons within the harmonic approximation (HA) and required anharmonic interatomic force constants (IFCs)

*y.zhao@ytu.edu.cn
†clian@utexas.edu
‡zhdai@ytu.edu.cn
§smeng@iphy.ac.cn

has failed to gain the correct κ_L in these structures due to the existence of imaginary phonon frequencies [17,18,27,28]. Hence, the inclusion of lattice anharmonicity in phonon eigenvalues is the first factor to consider in calculations of the κ_L for these perovskites. In past decades, several methods have been developed to calculate the finite-temperature anharmonic phonons by including lattice anharmonic effect [29–33]. Among these methods, the self-consistent phonon (SCP) theory in Ref. [33] is the one programed in an *ab initio* manner recently [27,34]. Combined with the compressive sensing (CS) lattice dynamics that can train the IFCs swiftly based on the required data set of displacements and forces [35–37], the SCP method is even capable of calculating anharmonic phonons quickly in very large systems [38], meeting the requirement of high-throughput computations [39].

Besides anharmonic phonon eigenvalues, another crucial factor to determine the κ_L is the phonon scattering induced by lattice anharmonicity. In general, the solution of BTE with the inclusion of three-phonon (3ph) scattering arising from cubic (third-order) IFCs is adopted to obtain the κ_L in crystalline compounds, which successfully uncovers the microscopic mechanism underlying both high and low κ_L [40–46]. However, the consideration of only 3ph scattering sometimes leads to a much higher κ_L [40,47] than the experimental value [48,49]. In this case, the addition of four-phonon (4ph) scattering caused by quartic (fourth-order) IFCs gives a lowered κ_L that is comparable to the experimental result [50], indicating the necessity of quartic anharmonicity. In fact, the frequency shifts of anharmonic phonons relative to the harmonic ones are also contributed primarily by quartic anharmonicity. This can be interpreted from the perspective of phonon self-energy [51]. In energy, quartic anharmonicity gives rise to first-order correction to phonons, while second-order correction is dominated by cubic anharmonicity [27]. If the used anharmonic theory, e.g., the SCP method [33], only refers to first-order correction, the entire phonon frequency shift is formed by quartic anharmonicity. Therefore, the complete treatment of quartic anharmonicity, which includes 4ph scattering and phonon frequency shift, is of vital significance in calculations of accurate κ_L, especially for the compounds with lattice instability and strong 4ph scattering.

In view of the foregoing, we use a first-principles calculation method that combines the SCP theory, CS lattice dynamics, and BTE in this paper to calculate the κ_L with the inclusion of both 3ph and 4ph scatterings in a series of perovskites. The BTE is solved on top of SCP theory for the inclusion of a phonon frequency shift caused by quartic anharmonic renormalization. We focus on 16 cubic oxide and fluoride perovskites ($BaHfO_3$, $BaZrO_3$, $SrTiO_3$, $BaTiO_3$, $SrSiO_3$, $RbCaF_3$, $CsSrF_3$, $CsCaF_3$, $KMgF_3$, $BaLiF_3$, $RbCdF_3$, $RbMgF_3$, $KZnF_3$, $CsCdF_3$, $RbZnF_3$, and $CsHgF_3$) which are the most common structures able to exist at room temperature. Except cubic $SrTiO_3$, the values of κ_L from 100 K to 1000 K are calculated for each structure. Thermal conductivity spectrum $\kappa_L(\omega)$, scattering processes, and phase space, etc. are analyzed to uncover the underlying mechanism of heat conduction. Our results show that the complete treatment of quartic anharmonicity is indispensable to obtain a rational κ_L and its temperature dependence. In particular, the structures with lower κ_L have stronger 4ph scatterings that are comparable to or even exceed those of the 3ph processes.

II. METHODOLOGY

From the solution of phonon BTE [52], the κ_L along the α axis is computed as

$$\kappa_L^{\alpha\alpha} = \frac{\hbar^2}{k_B T^2 \Omega N_q} \sum_{\mathbf{q}\nu} n_{\mathbf{q}\nu}(n_{\mathbf{q}\nu}+1)\omega_{\mathbf{q}\nu}^2 v_{\mathbf{q}\nu}^{\alpha} F_{\mathbf{q}\nu}^{\alpha}, \tag{1}$$

where $\hbar$, k_B, T, Ω, and N_q are the reduced Planck's constant, Boltzmann constant, absolute temperature, volume of the unit cell, and the number of sampled $\mathbf{q}$ wave vectors, respectively. $\omega_{\mathbf{q}\nu}$ and $n_{\mathbf{q}\nu}$ are the frequency and population of the phonon mode $|\mathbf{q}\nu\rangle$ with mode index ν. $v_{\mathbf{q}\nu}^{\alpha}$ is the group velocity along the α axis, and $F_{\mathbf{q}\nu}^{\alpha}$ is written as

$$F_{\mathbf{q}\nu}^{\alpha} = \tau_{\mathbf{q}\nu}\left(v_{\mathbf{q}\nu}^{\alpha} + \Delta_{\mathbf{q}\nu}\right), \tag{2}$$

where $\tau_{\mathbf{q}\nu}$ is the lifetime of mode $|\mathbf{q}\nu\rangle$ under single-mode relaxation time approximation (SMRTA), $\Delta_{\mathbf{q}\nu}$ works only for the iterative solution of BTE and is a quantity displaying the population deviation of phonons from the SMRTA scheme.

Normally, except $\tau_{\mathbf{q}\nu}$ and $\Delta_{\mathbf{q}\nu}$, all phonon properties can be calculated within the HA by diagonalization of dynamic matrix transformed from harmonic IFCs. The computation of $\tau_{\mathbf{q}\nu}$ and $\Delta_{\mathbf{q}\nu}$ requires at least 3ph scattering process, which is generally computed by dealing with cubic anharmonicity in a perturbation way to the HA [53], as described by Eqs. (5)–(9) in Ref. [54]. These approximations offer the most common model of the κ_L, hereinafter referred to as HA + 3ph and κ_{3ph}^{HA} for resulting κ_L. After addition of quartic anharmonicity, there are three other models of the κ_L. First, if only 4ph scattering processes that will modify $\tau_{\mathbf{q}\nu}$ and $\Delta_{\mathbf{q}\nu}$ are added (see Eqs. (2)–(7) in Ref. [55] for the expressions of $\tau_{\mathbf{q}\nu}$ and $\Delta_{\mathbf{q}\nu}$ with the inclusion of both 3ph and 4ph scatterings), the HA + 3ph model is changed into the HA + 3, 4ph one, namely, $\kappa_{3,4ph}^{HA}$. Second, $\omega_{\mathbf{q}\nu}$ and $v_{\mathbf{q}\nu}$ become temperature dependent when phonon frequency shifts arising from quartic anharmonic renormalization are taken into account. We choose the SCP method to calculate the quartic anharmonic phonon here and, consequently, the abbreviated SCP + 3ph and κ_{3ph}^{SCP} are used to represent the κ_L calculated on top of the SCP theory with the inclusion of only 3ph scatterings. Finally, we label SCP + 3, 4ph and $\kappa_{3,4ph}^{SCP}$ as the resultant κ_L which includes complete quartic anharmonicity in addition to the 3ph scattering processes.

The calculation flow chart of the four kinds of lattice thermal conductivities κ_{3ph}^{HA}, $\kappa_{3,4ph}^{HA}$, κ_{3ph}^{SCP}, and $\kappa_{3,4ph}^{SCP}$ is plotted in Fig. 1. The first step is structural optimization of a primitive cell carried out by first-principles density functional theory (DFT) [56]. Then computations of dielectric tensors and Born effective charges needed for the nonanalytic part of the dynamical matrix are performed in the optimized primitive cell by density functional perturbation theory (DFPT) [57]. For required IFCs, both harmonic and anharmonic ones can be extracted from the CS lattice dynamics, in principle. To gain more precise harmonic IFCs, here we use the finite-displacement approach with a displacement of 0.01 Å to generate the perturbed structures whose forces are computed

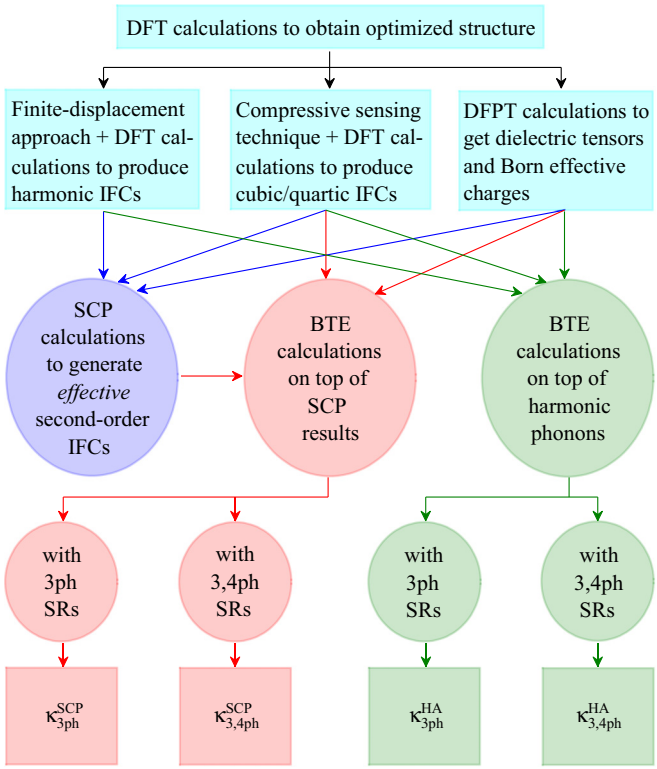

FIG. 1. Calculation flow chart of the four different kinds of lattice thermal conductivities κ^{HA}_{3ph}, $\kappa^{HA}_{3,4ph}$, κ^{SCP}_{3ph}, and $\kappa^{SCP}_{3,4ph}$.

subsequently by the static DFT. For cubic and quartic IFCs, the combination of CS lattice dynamics and static DFT is used to accelerate the computations, in which the anharmonic terms are trained by using the least absolute shrinkage and selection operator technique [27,47] based on a data set of displacements and forces extracted from the DFT calculations for chosen quasirandom configurations. With the gained dielectric tensors, Born effective charges, and harmonic to quartic IFCs as inputs, the κ^{HA}_{3ph} or $\kappa^{HA}_{3,4ph}$ is calculated directly by the solution of BTE with 3ph or 3,4ph scatterings. For calculations of κ^{SCP}_{3ph} and $\kappa^{SCP}_{3,4ph}$, the SCP computations are first performed based on dielectric tensors, Born effective charges, and harmonic and quartic IFCs, and then the real-space effective second-order IFCs at each considered temperature are obtained by Fourier transformation from the temperature-dependent anharmonic dynamical matrices produced by the SCP computations. Finally, the effective second-order IFCs at each temperature are used to replace the harmonic IFCs to solve the BTE, which generate the results of κ^{SCP}_{3ph} or $\kappa^{SCP}_{3,4ph}$ according to the inclusion of 3ph or 3,4ph scattering rates (SRs), as shown in Fig. 1.

All of the required DFT calculations are performed by using VASP [58,59], with the projector augmented wave potentials [60], the generalized gradient approximation (GGA) functional of Perdew-Burke-Ernzerhof (PBE) [61], and a cutoff energy of 520 eV. For structural optimization, the convergence criteria for ionic and electronic steps are set to be 10^{-6} eV/Å and 10^{-8} eV, respectively. The needed harmonic and anharmonic IFCs are produced within a $2 \times 2 \times 2$ supercell, and four configurations are generated by the finite-displacement approach coded in the ALAMODE package [27,34] for harmonic IFCs in each cubic perovskite. To select quasirandom configurations used for training the cubic and quartic IFCs by CS techniques, a 4000-step *ab initio* molecular dynamics (MD) is simulated at 300 K first, in which the set time step is 2 fs and the canonical ensemble with a chosen Nosé mass controlling the Nosé frequency to be similar to average phonon frequency is utilized. Then, 80 snapshots are sampled from the MD simulations and every atom in each sampled snapshot is displaced by 0.12 Å along a random direction, and, finally, the required quasirandom configurations used in subsequent static DFT calculations to produce the data set of displacements and forces are obtained. In the immediate CS lattice dynamics calculations, the anharmonic IFCs up to sixth order, the interactions up to sixth (third)-nearest neighbors for cubic (quartic) IFCs, and the nearest-neighbor interactions for quintic and sextic IFCs are considered. Since the accuracy of anharmonic IFCs is determined by the size of the training data set, sufficient snapshots should be sampled from the MD trajectories. Our test shows that 80 snapshots, which are twice those used in previous work for cubic $SrTiO_3$ [27], are sufficient enough to obtain the anharmonic IFCs that produce convergent anharmonic phonons and κ_L, and the fitting error for each cubic perovskite is less than 2%. In addition, all the DFT calculations are carried out within a $12 \times 12 \times 12$ ($6 \times 6 \times 6$) **k**-mesh for the primitive cells ($2 \times 2 \times 2$ supercells).

The SCP calculations are performed by employing the ALAMODE package. Due to the usages of $2 \times 2 \times 2$ supercells for producing the IFCs, a fixed $2 \times 2 \times 2$ **q**-mesh is utilized in the reciprocal-to-real-space Fourier interpolation, and consequently a much dense $\mathbf{q}_1$-mesh of $8 \times 8 \times 8$, which is applied to the inner loop of the SCP equation, as shown by Eqs. (20)–(23) in Ref. [27], is used to achieve the convergence of anharmonic phonon eigenvalues. The off-diagonal elements of phonon self-energies are included, and the mixing parameter of 0.1 is selected in the SCP iteration for all considered temperatures. The FOURPHONON package [50,55,74], a revised version of the SHENGBTE code [54], is employed for the solution of the phonon BTE. A uniform $12 \times 12 \times 12$ **q**-point mesh with a Gaussian smearing (scalebroad parameter) of 0.05 is chosen to simulate the phonon wave vectors and related integrals, which gives rises to about 2.2×10^6 3ph allowed processes and 1.6×10^{10} 4ph allowed processes. In addition, the BTE are solved in an iterative scheme for 3ph scatterings but with 4ph scatterings treated by SMRTA, since the iterative solution of 4ph processes will require huge computational costs [55].

III. RESULTS AND DISCUSSION

We focus on 16 cubic oxide and fluoride perovskites ABX_3 ($BaHfO_3$ [62], $BaZrO_3$ [63,75], $SrTiO_3$ [64,76,77], $BaTiO_3$ [65,78], $SrSiO_3$ [66], $RbCaF_3$ [67,79], $CsSrF_3$ [65,80], $CsCaF_3$ [67,81], $KMgF_3$ [68,79], $BaLiF_3$ [69,82,83], $RbCdF_3$ [65,70], $RbMgF_3$ [71,84], $KZnF_3$ [72,79,85], $CsCdF_3$ [70], $RbZnF_3$ [73,86], and $CsHgF_3$ [65,87]) that can exist at room temperature. The calculated lattice constants, dielectric tensors, and Born effective charges for these perovskites are listed in Table I, in which the 16 selected perovskites are

TABLE I. Calculated lattice constants ($a^{\rm opt}$), dielectric tensors (ϵ^{∞}), Born effective charges (Z^*), and temperature dependence of four kinds of lattice thermal conductivities $\kappa_{\rm 3ph}^{\rm HA}$, $\kappa_{\rm 3,4ph}^{\rm HA}$, $\kappa_{\rm 3ph}^{\rm SCP}$, and $\kappa_{\rm 3,4ph}^{\rm SCP}$ for the 16 cubic perovskites ABX_3 sorted first by oxides and fluorides and then by the increasing tolerance factor t. The experimental lattice constants $a^{\rm expt}$ are also listed for comparison. The temperature dependence is estimated from the values of $\kappa_{\rm 3ph}^{\rm HA}$, $\kappa_{\rm 3,4ph}^{\rm HA}$, $\kappa_{\rm 3ph}^{\rm SCP}$, and $\kappa_{\rm 3,4ph}^{\rm SCP}$ at temperatures $T \geqslant 200$ K for each structure, excluding the cubic $RbCaF_3$ in which thermal conductivity results at $T \geqslant 400$ K are used to gain the temperature dependence.

	t	$a^{\rm opt}$ (Å)	$a^{\rm expt}$ (Å)	ϵ^{∞}	Z^*(A)	Z^*(B)	$Z^*(\rm X)_{\parallel}$	$Z^*(\rm X)_{\perp}$	$\kappa_{\rm 3ph}^{\rm HA} \sim$	$\kappa_{\rm 3,4ph}^{\rm HA} \sim$	$\kappa_{\rm 3ph}^{\rm SCP} \sim$	$\kappa_{\rm 3,4ph}^{\rm SCP} \sim$
$BaHfO_3$	0.904	4.20	4.17 [62]	4.64	2.74	5.80	−4.55	−2.00	$T^{-0.95}$	$T^{-1.25}$	$T^{-0.85}$	$T^{-1.07}$
$BaZrO_3$	0.904	4.24	4.19 [63]	4.87	2.72	6.13	−4.86	−1.99	$T^{-0.95}$	$T^{-1.28}$	$T^{-0.81}$	$T^{-0.98}$
$SrTiO_3$	0.919	3.94	3.91 [64]	6.33	2.55	7.37	−5.87	−2.02	–	–	$T^{-0.61}$	$T^{-0.79}$
$BaTiO_3$	0.972	4.03	4.01 [65]	6.77	2.73	7.45	−5.92	−2.13	–	–	$T^{-0.39}$	$T^{-0.49}$
$SrSiO_3$	1.081	3.70	3.66 [66]	3.98	2.61	4.28	−3.26	−1.82	$T^{-1.09}$	$T^{-1.26}$	$T^{-0.91}$	$T^{-1.08}$
$RbCaF_3$	0.876	4.51	4.46 [67]	2.12	1.21	2.35	−1.64	−0.96	–	–	$T^{-0.60}$	$T^{-0.82}$
$CsSrF_3$	0.877	4.83	4.75 [65]	2.20	1.28	2.43	−1.67	−1.02	–	–	$T^{-0.38}$	$T^{-0.61}$
$CsCaF_3$	0.953	4.58	4.53 [67]	2.31	1.31	2.41	−1.58	−1.07	$T^{-0.90}$	$T^{-1.34}$	$T^{-0.70}$	$T^{-1.01}$
$KMgF_3$	0.955	4.04	3.99 [68]	2.05	1.18	2.01	−1.27	−0.96	$T^{-0.98}$	$T^{-1.11}$	$T^{-0.79}$	$T^{-0.99}$
$BaLiF_3$	0.961	4.04	3.99 [69]	2.57	2.71	1.05	−1.05	−1.36	$T^{-0.93}$	$T^{-1.30}$	$T^{-0.60}$	$T^{-0.91}$
$RbCdF_3$	0.983	4.49	4.40 [70]	2.39	1.22	2.37	−1.75	−0.92	–	–	$T^{-0.31}$	$T^{-0.57}$
$RbMgF_3$	1.008	4.10	4.01 [71]	2.17	1.24	2.07	−1.26	−1.03	$T^{-1.02}$	$T^{-1.34}$	$T^{-0.86}$	$T^{-1.08}$
$KZnF_3$	1.032	4.13	4.06 [72]	2.35	1.19	2.32	−1.72	−0.90	$T^{-0.97}$	$T^{-1.39}$	$T^{-0.71}$	$T^{-0.96}$
$CsCdF_3$	1.069	4.55	4.47 [70]	2.59	1.32	2.45	−1.74	−1.02	$T^{-0.98}$	$T^{-1.40}$	$T^{-0.55}$	$T^{-0.95}$
$RbZnF_3$	1.089	4.18	4.14 [73]	2.48	1.25	2.38	−1.72	−0.95	$T^{-1.02}$	$T^{-1.34}$	$T^{-0.67}$	$T^{-0.97}$
$CsHgF_3$	1.096	4.66	4.57 [65]	3.21	1.31	2.73	−2.14	−0.94	–	–	$T^{-0.50}$	$T^{-0.67}$

sorted first by oxides and fluorides and then by the increasing tolerance factor $t = (r_{\rm A} + r_{\rm X})/[\sqrt{2}(r_{\rm B} + r_{\rm X})]$, where $r_{\rm A}$, $r_{\rm B}$, and $r_{\rm X}$ represent the radii of A cation, B cation, and X anion, respectively. We find that the PBE optimizations give the lattice constants higher about $0.5\% - 2.0\%$ than the experimental values, consistent with the fact that GGA calculations tend to slightly overestimate the lattice constants. To check the rationality of calculated dielectric tensors ϵ^{∞} and Born effective charges Z^*, the results of cubic $SrTiO_3$ are used to compare with previous works. As listed in Table I, we obtain the values of $\epsilon^{\infty} = 6.33$, $Z^*(\rm Sr) = 2.55$, $Z^*(\rm Ti) = 7.37$, $Z^*(\rm O)_{\parallel} = -5.87$, and $Z^*(\rm O)_{\perp} = -2.02$ for cubic $SrTiO_3$, which are in well accordance with the previous computational values [27,88].

The calculated lattice thermal conductivities $\kappa_{\rm 3ph}^{\rm HA}$, $\kappa_{\rm 3,4ph}^{\rm HA}$, $\kappa_{\rm 3ph}^{\rm SCP}$, and $\kappa_{\rm 3,4ph}^{\rm SCP}$ as functions of temperature T from 100 to 1000 K for each selected cubic perovskite with naturally occurring isotope concentrations are plotted in Fig. 2. For the six cubic perovskites with imaginary HA phonon modes (see Fig. 9 for phonon spectra within the HA and SCP approximation), only the values of $\kappa_{\rm 3ph}^{\rm SCP}$ and $\kappa_{\rm 3,4ph}^{\rm SCP}$ are provided, since the solutions of $\kappa_{\rm L}$ within the HA are numerically invalid in these structures. For cubic $SrTiO_3$, the $\kappa_{\rm 3ph}^{\rm SCP}$ and $\kappa_{\rm 3,4ph}^{\rm SCP}$ at 100 K are absent because a cubic-to-tetragonal phase transition accompanied with the freezing-out of the antiferrodistortive (AFD) soft mode occur at 105 K in this material [23,24]. The experimental thermal conductivities $\kappa^{\rm expt}$ for cubic $BaHfO_3$, $BaZrO_3$, $SrTiO_3$, $RbCaF_3$, $KMgF_3$, and $KZnF_3$ are also plotted for comparison, which are adapted from the data in Refs. [62,63,77,79]. To further reveal the nature of heat conduction, a power law of $\kappa_{\rm L} \propto T^{-\alpha}$ is used to describe the temperature dependence of $\kappa_{\rm L}$. Since the $\kappa_{\rm L}$ at very low temperature is dominated by the lattice specific heat with a T^3 law at the low-temperature limit, we estimate the temperature dependence here from the values of $\kappa_{\rm L}$ at temperatures $T \geqslant 200$ K for all selected perovskites, except cubic $RbCaF_3$, in which the temperature dependence is captured at $T \geqslant 400$ K, as listed in Table I.

We start from the $\kappa_{\rm 3ph}^{\rm HA}$ in the ten cubic perovskites being stable within the HA, as shown in Fig. 2. One can find that the calculated $\kappa_{\rm 3ph}^{\rm HA}$ in cubic $BaHfO_3$, $BaZrO_3$, and $KMgF_3$ agree with the experimental values, while the $\kappa_{\rm 3ph}^{\rm HA}$ in cubic $KZnF_3$ are much lower than the experimental results. Compared with the calculated $\kappa_{\rm 3ph}^{\rm HA}$ in cubic $BaHfO_3$, $SrSiO_3$, $KMgF_3$, and $RbMgF_3$, the solutions of $\kappa_{\rm 3ph}^{\rm HA}$ in cubic $BaLiF_3$, $KZnF_3$, $CsCdF_3$, and $RbZnF_3$ produce relatively smaller values, e.g., 2.29, 2.65, 1.49, and 2.60 W/mK, respectively, at room temperature, comparable to the $\kappa_{\rm L} \sim 2$ W/mK in typical thermoelectric material PbTe [89,90]. As listed in Table I, we capture a temperature dependence of $\kappa_{\rm 3ph}^{\rm HA} \sim T^{-\alpha}$ with $\alpha \sim 0.9 - 1.09$ in the ten perovskites being stable within the HA, which is consistent with the universal law of $\kappa_{\rm L} \sim T^{-1}$ in common semiconductors. Then we discuss the nature of $\kappa_{\rm 3,4ph}^{\rm HA}$. With the addition of 4ph scatterings via the SMRTA scheme into the $\kappa_{\rm 3ph}^{\rm HA}$, the obtained $\kappa_{\rm 3,4ph}^{\rm HA}$ underestimate the $\kappa_{\rm L}$ compared with the values of $\kappa_{\rm 3ph}^{\rm HA}$. As a result, the $\kappa_{\rm 3,4ph}^{\rm HA}$ are much smaller than experimental results in cubic $BaHfO_3$, $BaZrO_3$, $KMgF_3$, and $KZnF_3$, indicating the deficiency of this $\kappa_{\rm L}$-theory for these perovskites. Meanwhile, a strengthened temperature dependence of $\kappa_{\rm 3,4ph}^{\rm HA} \sim T^{-\alpha}$ with $\alpha \sim 1.11 - 1.40$ is captured, further verifying the limitation of the $\kappa_{\rm 3,4ph}^{\rm HA}$ theory for these materials.

The solutions of $\kappa_{\rm L}$ including phonon frequency shifts caused by quartic anharmonic renormalization become numerically valid in all selected perovskites, regardless of whether only 3ph scatterings or both 3ph and 4ph scatterings

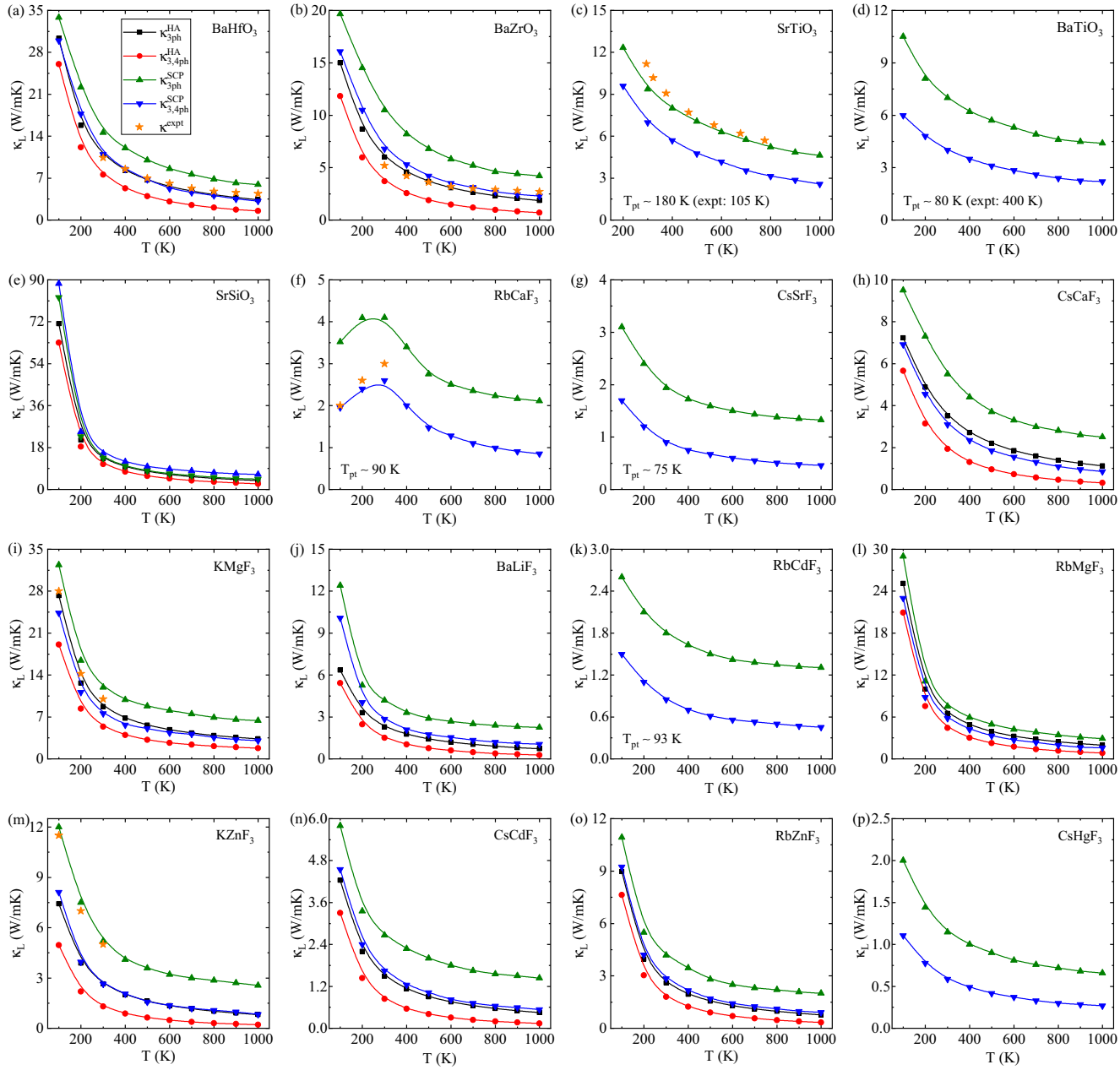

FIG. 2. Four kinds of lattice thermal conductivities κ_{3ph}^{HA}, $\kappa_{3,4ph}^{HA}$, κ_{3ph}^{SCP}, and $\kappa_{3,4ph}^{SCP}$ versus temperature T for 16 naturally occurring cubic perovskites: (a) $BaHfO_3$, (b) $BaZrO_3$, (c) $SrTiO_3$, (d) $BaTiO_3$, (e) $SrSiO_3$, (f) $RbCaF_3$, (g) $CsSrF_3$, (h) $CsCaF_3$, (i) $KMgF_3$, (j) $BaLiF_3$, (k) $RbCdF_3$, (l) $RbMgF_3$, (m) $KZnF_3$, (n) $CsCdF_3$, (o) $RbZnF_3$, and (p) $CsHgF_3$. The black square, red circle, green triangle, and blue nabla lines represent the κ_{3ph}^{HA}, $\kappa_{3,4ph}^{HA}$, κ_{3ph}^{SCP}, and $\kappa_{3,4ph}^{SCP}$, respectively. The experimental lattice thermal conductivities κ^{expt} in (a), (b), (c), (f), (i), and (m) are labeled by the orange pentagram, which are adapted from Ref. [62], Ref. [63], Ref. [77], Ref. [79], Ref. [79], and Ref. [79], respectively. In (c), (d), (f), (g), and (k), the calculated phase transition temperature T_{pt}, below which the cubic structural phase cannot exist, is also labeled, and the value in parenthesis is the experimental result.

are involved. We concentrate on the κ_{3ph}^{SCP} first. In sharp contrast to the $\kappa_{3,4ph}^{HA}$, the solutions of κ_{3ph}^{SCP} in the ten perovskites stable within the HA generate the overestimated κ_L relative to the results of κ_{3ph}^{HA}, accompanying with a weakened temperature dependence of $\kappa_{3ph}^{SCP} \sim T^{-\alpha}$ with $\alpha \sim 0.55 - 0.91$. Strikingly, the calculated κ_{3ph}^{SCP} in some of the six perovskites with imaginary HA phonons exhibits an anomalously weak temperature dependence, e.g., $\kappa_{3ph}^{SCP} \sim T^{-\alpha}$ with $\alpha \sim 0.31 - 0.39$ for cubic $BaTiO_3$, $CsSrF_3$, and $RbCdF_3$, as listed in Table I. Then the κ_L with complete quartic anharmonic effect is discussed. As plotted in Fig. 2, the addition of 4ph scatterings on the basis of κ_{3ph}^{SCP} evidently reduces the resultant κ_L and, consequently, the obtained $\kappa_{3,4ph}^{SCP}$ have the values close to those of κ_{3ph}^{HA} and a reasonable temperature dependence of $\kappa_{3,4ph}^{SCP} \sim T^{-\alpha}$ with $\alpha \sim 0.91 - 1.08$ in the ten perovskites stable within the HA.

In theory, due to full inclusion of quartic anharmonicity, the results of $\kappa_{3,4ph}^{SCP}$ should be the most accurate κ_L. Therefore, the calculated $\kappa_{3,4ph}^{SCP}$ agree well with the experimental values in cubic $BaHfO_3$, $BaZrO_3$, $KMgF_3$, and $RbCaF_3$, especially in cubic $RbCaF_3$ where a declined trend of $\kappa_{3,4ph}^{SCP}$ with decreasing temperature at $T \leqslant 300$ K is also consistent with the experimental κ_L trend, which will be interpreted later. Moreover, the remarkably low κ_L can be obtained from the solutions of $\kappa_{3,4ph}^{SCP}$ in some perovskites with imaginary HA phonons. For instance, the room-temperature values of $\kappa_{3,4ph}^{SCP}$ in cubic $CsSrF_3$, $RbCdF_3$, and $CsHgF_3$ are 0.90, 0.85, and 0.59 W/mK, respectively, as shown in Figs. 2(g), 2(k), and 2(p), which are comparable to the results of $\kappa_L \sim 0.5 - 1.0$ W/mK in the full Heusler semiconductors [12].

However, the $\kappa_{3,4ph}^{SCP}$ in cubic $SrTiO_3$ and $KZnF_3$ are evidently lower than the experimental results, as shown in Figs. 2(c) and 2(m). There are three potential reasons for the inconsistency between the calculated $\kappa_{3,4ph}^{SCP}$ and experimental values in cubic $SrTiO_3$ and $KZnF_3$. First, the solution of $\kappa_{3,4ph}^{SCP}$ is performed with 4ph scattering processes treated by the SMRTA scheme, which maybe underestimate the κ_L for some materials with strong normal processes of 4ph scatterings [91,92]. To see whether the solution of $\kappa_{3,4ph}^{SCP}$ is reasonable here, the normal and Umklapp 4ph processes in cubic $SrTiO_3$ and $KZnF_3$ are analyzed, as shown in Fig. 10. We discover the Umklapp processes dominate the 4ph scatterings, signifying the suitableness of the SMRTA scheme in treating 4ph scatterings. Second, the used GGA-PBE functional tends to overestimate the lattice constant, which may also affect the final κ_L [17]. Therefore, we recalculate the κ_L by using the experimental lattice constants for cubic $SrTiO_3$ and $KZnF_3$, as plotted in Fig. 11, in which the calculated $\kappa_{3,4ph}^{SCP}$ are enhanced some but still lower than the experimental values. Last but not least, some samples in experiment maybe include a certain concentration of carries that will give rise to considerable electrical thermal conductivity κ_{el}, while the measured total thermal conductivity comprising κ_L and κ_{el} is usually taken as the κ_L for semiconductors. As an example, we roughly estimate the κ_{el} for some samples of cubic $SrTiO_3$ via Wiedemann-Franz formula $\kappa_{el} = L\sigma T$ (L is the Lorenz number with a value of 2.44×10^{-8} WΩ/K^2). As shown in Fig. 1 in Ref. [76], the largest electrical conductivity $\sigma \sim 10^5$ S/m can be captured at 300 K in some samples, which corresponds to a $\kappa_{el} \sim 0.732$ W/mK. If the κ_{el} is deducted from the experimental thermal conductivity, the calculated $\kappa_{3,4ph}^{SCP}$ becomes more closer to the revised values of κ_L^{expt}, although still somewhat lower than the revised results, as shown in Fig. 11(a). Anyhow, our calculations of κ_L with optimized lattice constants are analogous to the findings in previous work which exhibit the consistency of the calculated κ_{3ph}^{SCP} with the experimental values in cubic $SrTiO_3$ [27], and provide the cubic $KZnF_3$ as another example to possess the similar consistency, as shown in Figs. 2(c) and 2(m). Overall, for the six cubic perovskites with experimental thermal conductivities κ^{expt}, the inclusion of quartic anharmonicity, fully or only phonon frequency shifts, is indispensable to obtain the calculated κ_L consistent with the experimental results.

To uncover the quartic anharmonicity in many aspects, the ratios of $\kappa_{3,4ph}^{HA}/\kappa_{3ph}^{HA}$, $\kappa_{3ph}^{SCP}/\kappa_{3ph}^{HA}$, $\kappa_{3,4ph}^{SCP}/\kappa_{3ph}^{HA}$, and $\kappa_{3,4ph}^{SCP}/\kappa_{3ph}^{SCP}$ for values of the κ_L at room temperature are plotted in Fig. 3. According to four kinds of definition for the κ_L, we know that the ratio of $\kappa_{3,4ph}^{HA}/\kappa_{3ph}^{HA}$ reflects the effect of additional 4ph scatterings on the basis of 3ph processes, the value of $\kappa_{3ph}^{SCP}/\kappa_{3ph}^{HA}$ signifies the influence of phonon frequency shifts arising from quartic anharmonic renormalization, and the result of $\kappa_{3,4ph}^{SCP}/\kappa_{3ph}^{HA}$ indicates the full quartic anharmonic effect. $\kappa_{3,4ph}^{SCP}/\kappa_{3ph}^{SCP}$ has similar information to $\kappa_{3,4ph}^{HA}/\kappa_{3ph}^{HA}$ but can be applied in all structures, including the perovskites with imaginary HA phonons. As displayed in Fig. 3, $\kappa_{3,4ph}^{SCP}/\kappa_{3ph}^{SCP}$ in cubic $CsSrF_3$, $CsCaF_3$, $RbCdF_3$, $KZnF_3$, and $CsHgF_3$ have values in the range of $0.46 - 0.56$, which means that the SRs of 4ph are comparable to those of 3ph in these materials. Likewise, we can infer that cubic $BaZrO_3$, $CsCaF_3$, $BaLiF_3$, $CsCdF_3$, $KZnF_3$, and $RbZnF_3$ possess a strong effect of phonon frequency shifts from the ratio of $\kappa_{3ph}^{SCP}/\kappa_{3ph}^{HA}$ having large values, e.g., >1.5. In fact, the 4ph scatterings and phonon frequency shifts play competitive roles in the ultimate κ_L. In other words, the result of $\kappa_{3,4ph}^{SCP}/\kappa_{3ph}^{HA} \sim 1.0$ in cubic $BaHfO_3$ and $KZnF_3$ signifies that the contributions of 4ph scatterings and phonon frequency shifts to the $\kappa_{3,4ph}^{SCP}$ cancel each other out, while the relation of $\kappa_{3,4ph}^{SCP}/\kappa_{3ph}^{HA} < 1.0$ in cubic $CsCaF_3$, $KMgF_3$, and $RbMgF_3$ ($\kappa_{3,4ph}^{SCP}/\kappa_{3ph}^{HA} > 1.0$ in cubic $BaZrO_3$, $SrSiO_3$, $BaLiF_3$, $CsCdF_3$, and $RbZnF_3$) means larger contributions of 4ph scatterings (phonon frequency shifts) relative to those of phonon frequency shifts (4ph scatterings) to the $\kappa_{3,4ph}^{SCP}$.

Unlike previous works, from the ratio of $\kappa_{3,4ph}^{SCP}/\kappa_{3ph}^{SCP}$ we can find anomalously strong 4ph scatterings in some cubic perovskites, especially in the ones with imaginary HA phonons. To detect the relation between 4ph scatterings and resultant κ_L, the $\kappa_{3,4ph}^{SCP}$ as a function of the ratio $\kappa_{3,4ph}^{SCP}/\kappa_{3ph}^{SCP}$ at room temperature is plotted in Fig. 4. As a whole, we discover a roughly linear relation between $\kappa_{3,4ph}^{SCP}$ and the ratio $\kappa_{3,4ph}^{SCP}/\kappa_{3ph}^{SCP}$ in the 16 cubic perovskites, which displays that the structures with lower $\kappa_{3,4ph}^{SCP}$ have relatively smaller ratios of $\kappa_{3,4ph}^{SCP}/\kappa_{3ph}^{SCP}$ and thus stronger 4ph scatterings, as depicted by the data points in the orange zone in Fig. 4. In particular, cubic $CsSrF_3$ and $RbCdF_3$, with $\kappa_{3,4ph}^{SCP} < 1.0$ W/mK at 300 K, possess the 4ph scatterings even exceeding the 3ph ones, as proved by the results of $\kappa_{3,4ph}^{SCP}/\kappa_{3ph}^{SCP} < 0.5$ in these perovskites. In addition, all the structures with low $\kappa_{3,4ph}^{SCP}$, e.g., <3 W/mK, and small $\kappa_{3,4ph}^{SCP}/\kappa_{3ph}^{SCP}$, e.g., <0.6 are fluoride perovskites, as shown in Fig. 4.

In the following, we take cubic $BaHfO_3$ and $CsSrF_3$ as two examples with higher and lower κ_L, respectively, to investigate the role of quartic anharmonicity in the resultant κ_L in detail. The phonon spectra within the HA and SCP approximation for the two cubic perovskites are plotted in Figs. 5(a) and 5(d). Obviously, the HA phonon spectrum without imaginary frequency in cubic $BaHfO_3$ signifies the dynamical stability, while the low-lying HA modes around the M $(\frac{1}{2}, \frac{1}{2}, 0)$ and R $(\frac{1}{2}, \frac{1}{2}, \frac{1}{2})$ points in cubic $CsSrF_3$ are unstable, e.g., with an imaginary frequency of $52.4i$ $(57.1i)$ cm^{-1} for the softest mode at the M (R) point. In consideration of quartic anharmonic renormalization, the SCP phonon spectra in cubic $CsSrF_3$ have no imaginary frequency observed at the considered temperatures, due to the large frequency shifts of the low-lying phonon modes in this material, as shown in

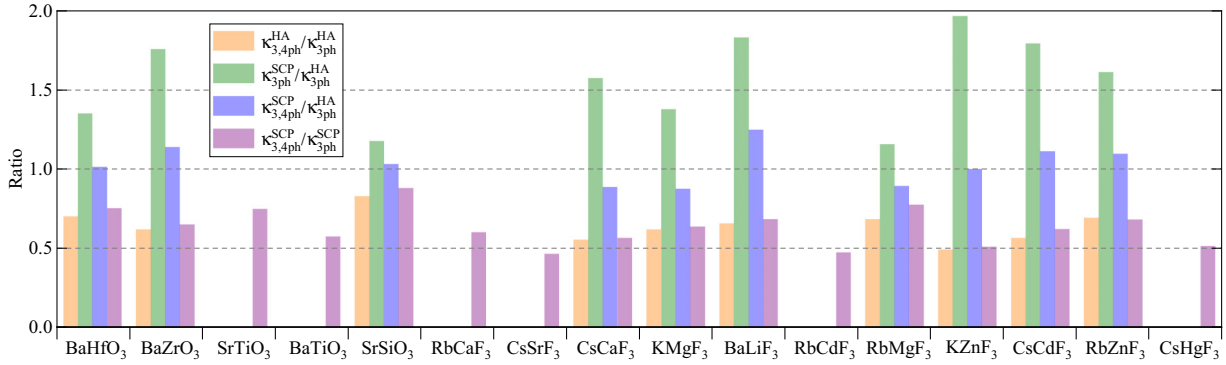

FIG. 3. The ratios of $\kappa^{HA}_{3,4ph}/\kappa^{HA}_{3ph}$, $\kappa^{SCP}_{3ph}/\kappa^{HA}_{3ph}$, $\kappa^{SCP}_{3,4ph}/\kappa^{HA}_{3ph}$, and $\kappa^{SCP}_{3,4ph}/\kappa^{SCP}_{3ph}$ calculated with the values at 300 K for the 16 cubic perovskites ABX_3.

Fig. 5(d). Meanwhile, the low-lying modes around the R point in cubic $BaHfO_3$ are also evidently hardened by the quartic anharmonicity, as shown in Fig. 5(a). Since the diagonal term of the quartic coefficient has a positive and dominant contribution to phonon eigenvalue, the quartic anharmonic effect generally boosts frequencies of the low-lying modes [27,47], which is observed in all 16 cubic perovskites, as shown in Fig. 9. In addition, due to widely different contribution from the quartic coefficient, the high-frequency modes have relatively weak quartic anharmonic renormalization in cubic $BaHfO_3$, $BaZrO_3$, $CsCaF_3$, $KZnF_3$, $CsCdF_3$, and $CsHgF_3$, small positive renormalization to phonons in cubic $SrTiO_3$, $BaTiO_3$, $SrSiO_3$, $KMgF_3$, $BaLiF_3$, $RbMgF_3$, and $RbZnF_3$, and small negative renormalization in cubic $RbCaF_3$, $CsSrF_3$, and $RbCdF_3$, as shown in Fig. 9.

For cubic $CsSrF_3$, to reveal the latent structural phase transition, we also focus on the variation of squared phonon frequencies ω^2 with temperature T for the softest low-lying mode at the R point, which corresponds to the well-known AFD mode in cubic $SrTiO_3$ [23,24]. Strictly speaking, the SCP frequency is unable to be used for predicting the phase transition temperature T_{pt} since it is always positive by definition, and thus the Hessian of the SCP free energy, which is detailed in Ref. [44] and references therein, should be adopted to investigate the phase transition. As a preliminary estimation, here we use the curve of ω^2 versus T for the softest low-lying mode and fit the linear region of the curve to predict a structural phase transition that offers a temperature below which the cubic structural phase cannot exist. We find from the fitting results that the ω^2 tends to zero at $T \sim 75$ K for the softest low-lying mode at the R point in cubic $CsSrF_3$, demonstrating the freezing out of this mode and presence of a potential structural phase transition, as shown in Fig. 12. Similar phenomenon is also discovered in cubic $BaTiO_3$, $RbCaF_3$, and $RbCdF_3$ at about 80, 90, and 93 K, respectively. The exception is that the used softest low-lying mode for cubic $BaTiO_3$ is situated at the Γ point, as shown in Fig. 10(d). To test the rationality of our estimations, the variation of ω^2 versus T for the AFD mode in cubic $SrTiO_3$ is also calculated, and the liner fitting results exhibit that this mode becomes freezing-out at about 180 K, which is higher than the cubic-to-tetragonal phase transition observed at 105 K in experiments [23,24], but agrees with previous similar calculations [27]. In addition, there is no freezing out of any soft mode in cubic $CsHgF_3$ at low temperatures according to the SCP computations, although the HA phonons display lattice instabilities in this material. In other words, the SCP computations always give stable phonons in this structure as long as the phonon frequency shifts arising from quartic anharmonicity is considered, meaning that the cubic $CsHgF_3$ can exist at any low temperatures. Given the fact that $BaTiO_3$ undergoes cubic, tetragonal, orthorhombic, and rhombohedral crystal structure from high to low temperature, we can further witness that the application of SCP frequency or its square is inadequate to reveal the true phase transition in some cases, and only the comparison of SCP free energies for every possible structural phase is reasonable to predict the true phase transition temperature T_{pt}. As an example, we discuss the cubic-to-tetragonal phase transition in $BaTiO_3$. The experimental T_{pt} of cubic-to-tetragonal transition for $BaTiO_3$ is about 400 K [93], which is much higher than the $T_{pt} \sim 80$ K estimated from linear fitting of the curve of SCP frequency square ω^2 versus T. Based on the SCP phonons, we emphasize here that the cubic phase of $BaTiO_3$ is able to exist at the temperature above 80 K, only it is a metastable structural phase until the temperature exceeds 400 K.

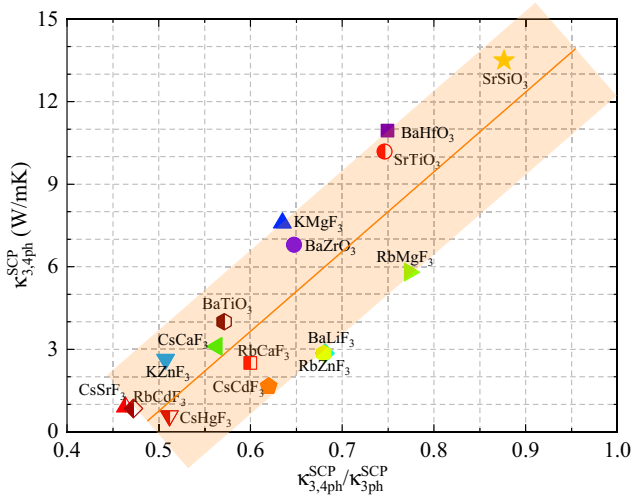

FIG. 4. The $\kappa^{SCP}_{3,4ph}$ as a function of the ratio $\kappa^{SCP}_{3,4ph}/\kappa^{SCP}_{3ph}$ at 300 K for the 16 cubic perovskites ABX_3. All data points are located in the orange zone.

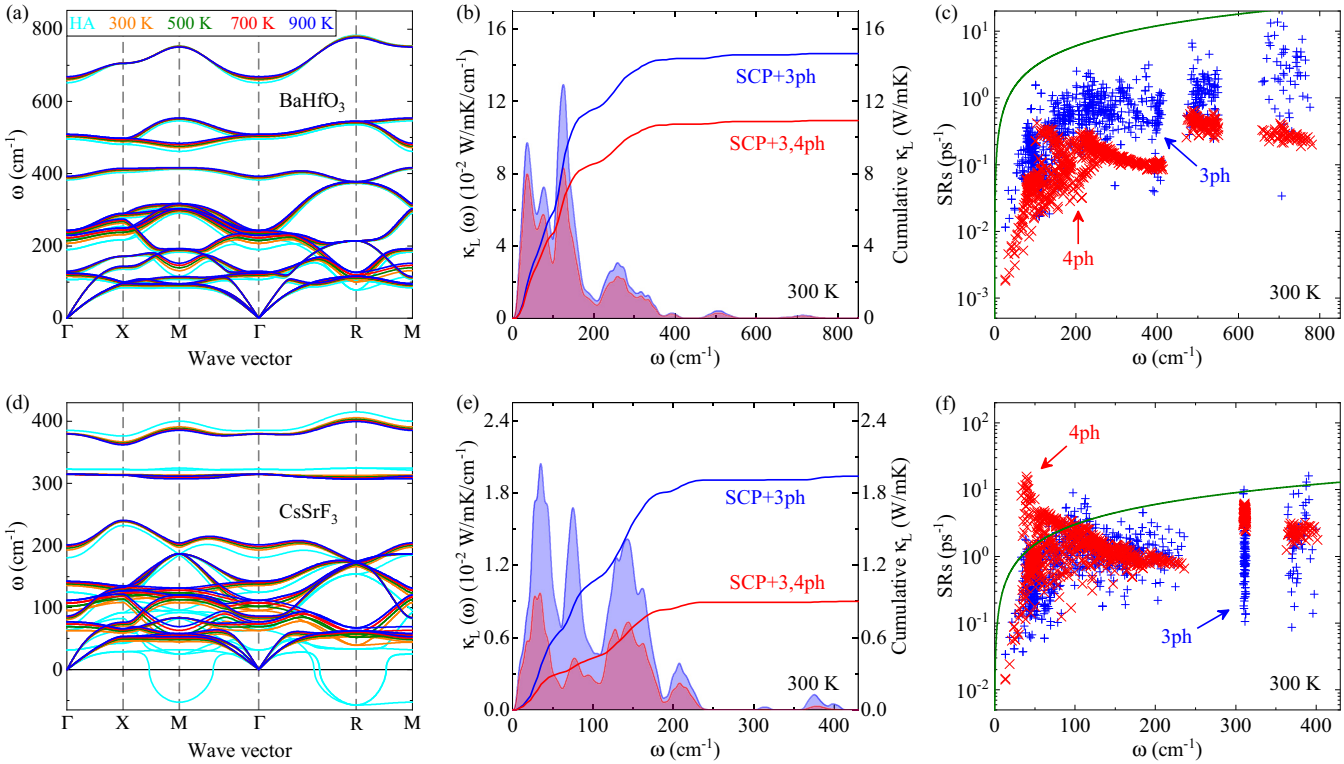

FIG. 5. (a) HA and SCP phonon spectra for cubic $BaHfO_3$. (b) Thermal conductivity spectra $\kappa_L(\omega)$ calculated within the SCP + 3ph and SCP + 3, 4ph models at 300 K (the curves below which the areas are filled) and corresponding cumulative κ_L (the bare curves) for cubic $BaHfO_3$. (c) 3ph and 4ph SRs at 300 K for cubic $BaHfO_3$. (d)–(f) Same as (a)–(c) but for cubic $CsSrF_3$. In (a) and (d), the cyan line represents the HA dispersion, and the orange, green, red, and blue lines denote the SCP dispersions at 300, 500, 700, and 900 K, respectively. The green curves in (c) and (f) indicate that the SRs equal to phonon frequencies, that is, $1/\tau = \omega/2\pi$.

To elucidate the origin of the κ_L and the role of 4ph scatterings, we analyze the thermal conductivity spectra $\kappa_L(\omega)$ calculated within the κ_{3ph}^{SCP} and $\kappa_{3,4ph}^{SCP}$ theories at room temperature and corresponding cumulative values for cubic $BaHfO_3$ and $CsSrF_3$, as shown in Figs. 5(b) and 5(e). One can find that low-frequency phonons, e.g., with the frequencies of $\omega < 400$ (200) cm^{-1} in cubic $BaHfO_3$ ($CsSrF_3$), carry the majority of lattice heat conduction. Meanwhile, the thermal conductivity spectra $\kappa_{3,4ph}^{SCP}(\omega)$ are evidently lowered with respect to the $\kappa_{3ph}^{SCP}(\omega)$ by the presence of 4ph scatterings, especially in cubic $CsSrF_3$. As a result, the cumulative values within the SCP + 3ph model exceed the ones within the SCP + 3, 4ph, and the final $\kappa_{3,4ph}^{SCP}$ is only about 75% (46%) of the κ_{3ph}^{SCP} in cubic $BaHfO_3$ ($CsSrF_3$). The 3ph and 4ph scattering processes at room temperature are compared in Figs. 5(c) and 5(f). We can see that the 4ph scattering processes in cubic $CsSrF_3$ are comparable to the 3ph ones and even exceed the 3ph ones in the frequency range of $30 - 85$ cm^{-1}, in line with the result of $\kappa_{3,4ph}^{SCP}/\kappa_{3ph}^{SCP} = 0.46$, while the 4ph scatterings are evidently lower than the 3ph ones in cubic $BaHfO_3$. Similar dominated situations of the 4ph processes are also found in cubic $BaTiO_3$, $RbCaF_3$, $CsCaF_3$, $RbCdF_3$, $KZnF_3$, and $CsHgF_3$, as shown in Fig. 13. Moreover, with the increase of temperature, the 4ph scatterings become more obviously stronger than the 3ph ones in cubic $CsSrF_3$, as shown in Fig. 14, in which the 4ph processes even in cubic $BaHfO_3$ are also comparable to the 3ph ones at the high temperature 900 K. To check the suitability of the phonon quasiparticle picture, the curve with SRs equal to phonon frequencies, that is, $1/\tau = \omega/2\pi$, which means the phonon lifetime τ is equivalent to the vibration period of phonon quasiparticle, is also plotted in Figs. 5(c), 5(f), 13, and 14. Once the SRs exceed the curve of $1/\tau = \omega/2\pi$, the phonon lifetime τ becomes less than one vibration period (phonon annihilates before completing one vibration), and thus the phonon quasiparticle picture is no longer effective. As shown in Figs. 5, 13, and 14, the majority of 3ph and 4ph scatterings are distributed below the curve of $1/\tau = \omega/2\pi$, supporting the validity of BTE solutions in this paper. To further probe the underlying mechanism of strong 4ph scatterings, the 3ph and 4ph scattering phase spaces (P_3 and P_4) at 300 K for cubic $BaHfO_3$ and $CsSrF_3$ are also analyzed, which indicates that the total P_4 in cubic $CsSrF_3$ are almost same as the total P_3, in contrast to the lower total P_4 relative to the total P_3 in cubic $BaHfO_3$, as shown in Figs. 15(a) and 15(b).

To explore more details of the 4ph scattering processes, the 4ph scatterings are decomposed into those arising from three individual processes, namely, splitting ($\lambda \rightarrow \lambda' + \lambda'' + \lambda'''$), redistribution ($\lambda + \lambda' \rightarrow \lambda'' + \lambda'''$), and recombination ($\lambda + \lambda' + \lambda'' \rightarrow \lambda'''$) processes, respectively, where λ is the abbreviation of mode $|\mathbf{q}\nu\rangle$. As shown in Figs. 6(a) and 6(c), the redistribution processes in both cubic $BaHfO_3$ and $CsSrF_3$ dominate over the other two processes, which can be interpreted in the perspective of their associated scattering phase spaces. Taking the constraint imposed by the conservation of phonon energies in scattering processes into account, one can

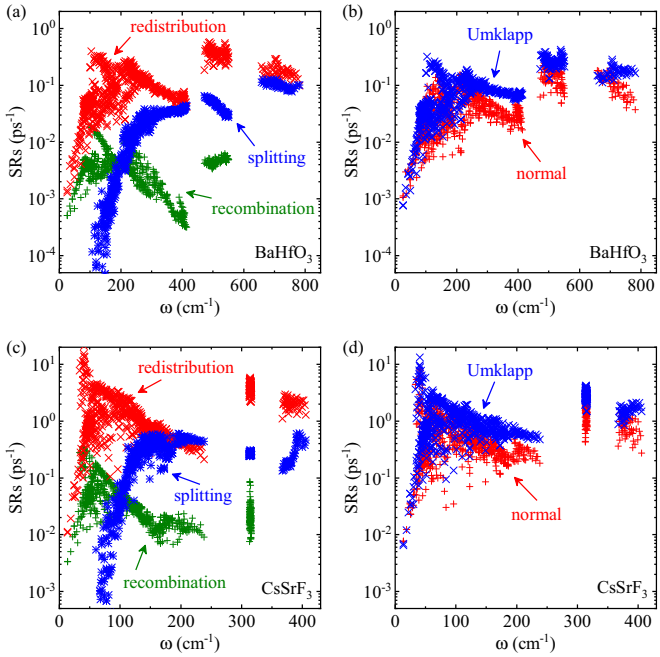

FIG. 6. (a) Decomposed 4ph scatterings into the splitting ($\lambda \rightarrow \lambda' + \lambda'' + \lambda'''$), redistribution ($\lambda + \lambda' \rightarrow \lambda'' + \lambda'''$), and recombination ($\lambda + \lambda' + \lambda'' \rightarrow \lambda'''$) processes for cubic $BaHfO_3$. (b) Decomposed 4ph scatterings into the normal and Umklapp processes for cubic $BaHfO_3$. (c) and (d) are same as (a) and (b), respectively, but for cubic $CsSrF_3$.

expect that the splitting processes are largely associated with the high-lying phonon modes while the recombination processes are more related to phonons with low frequencies. On the other hand, the redistribution processes are more flexible in satisfying the conservation of phonon energies, and thus contribute many more 4ph scattering events [94]. As a result, both scattering phase spaces and 4ph scatterings are dominated by the redistribution processes, as shown in Figs. 6(a), 6(c), 15(c), and 15(d). The 4ph scatterings can be also decomposed into normal and Umklapp processes. As plotted in Figs. 6(b) and 6(d), the Umklapp processes dominate over the normal ones in both cubic $BaHfO_3$ and $CsSrF_3$, analogous to the cases in cubic $KZnF_3$ and $SrTiO_3$ shown in Fig. 10. Similar dominated cases of the Umklapp processes can also be found in other structures of the 16 cubic perovskites, as shown in Fig. 10, which signifies the rationality of the SMRTA scheme used in solutions of the BTE to treat the 4ph scattering processes for all 16 materials.

In addition, the phonon frequencies $\omega_{\mathbf{q}\nu}$ and group velocities $v_{\mathbf{q}\nu}$ are also the commonly used physical quantities to reveal the origin of different κ_L. From the HA results to the SCP ones, both $\omega_{\mathbf{q}\nu}$ and $v_{\mathbf{q}\nu}$ are usually enhanced in the low-frequency range governing the κ_L by the quartic anharmonic renormalization. Moreover, the enhancements become more evident at high temperature, according to the SCP calculations, as exhibited by the $v_{\mathbf{q}\nu}$ in cubic $BaHfO_3$ and $CsSrF_3$ in Fig. 16. The difference is that the low-frequency $v_{\mathbf{q}\nu}$ within the SCP at 300 K in cubic $CsSrF_3$ are lower by about 30% than those in cubic $BaHfO_3$, which, combined with the much stronger 3,4ph scatterings in cubic $CsSrF_3$ relative to those in

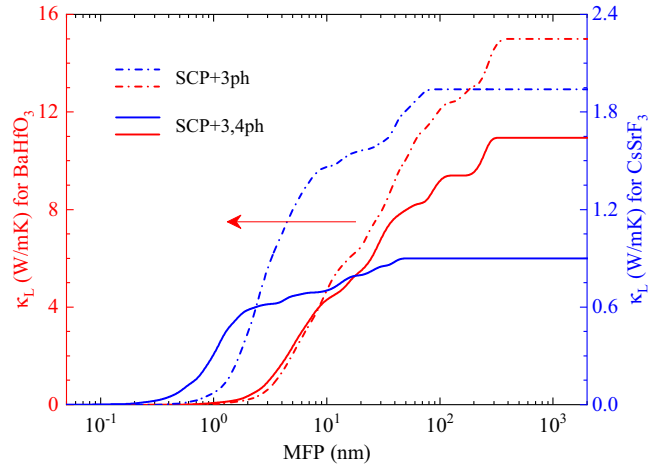

FIG. 7. The MFP cumulative κ_L for cubic $BaHfO_3$ and $CsSrF_3$. The red and blue lines denote the results for cubic $BaHfO_3$ and $CsSrF_3$, which are scaled by the left and right rims, respectively. The dash dot lines represent the results within SCP + 3ph model, and the full lines denote the values within SCP + 3, 4ph one.

cubic $BaHfO_3$, gives rise to the ultimate $\kappa^{SCP}_{3,4ph}$ in cubic $CsSrF_3$ about an order of magnitude lower than that in cubic $BaHfO_3$.

Then we discuss the κ_L with respect to the allowed phonon maximum mean-free path (MFP), namely, the MFP cumulative κ_L, within the SCP + 3ph and SCP + 3, 4ph models to indicate the effect of 4ph processes on the size dependence of heat conduction. The MFP cumulative κ_L at 300 K for cubic $BaHfO_3$ and $CsSrF_3$ is plotted in Fig. 7. Within the SCP + 3ph (SCP + 3, 4ph) approximation, the total

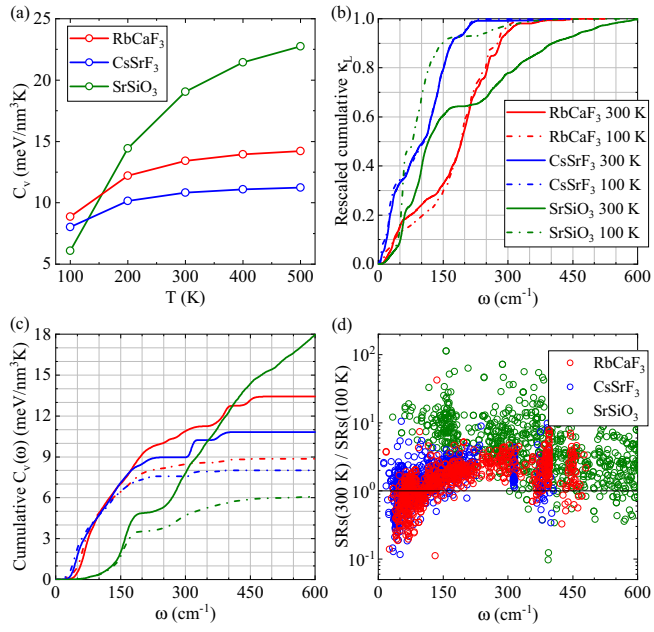

FIG. 8. (a) Total specific heats C_v, (b) rescaled cumulative κ_L at 100 and 300 K, (c) cumulative $C_v(\omega)$ at 100 and 300 K, and (d) ratios of total SRs between 100 and 300 K calculated within the SCP + 3, 4ph model for cubic $RbCaF_3$, $CsSrF_3$, and $SrSiO_3$. The curves in (c) have the same color legends as those in (b).

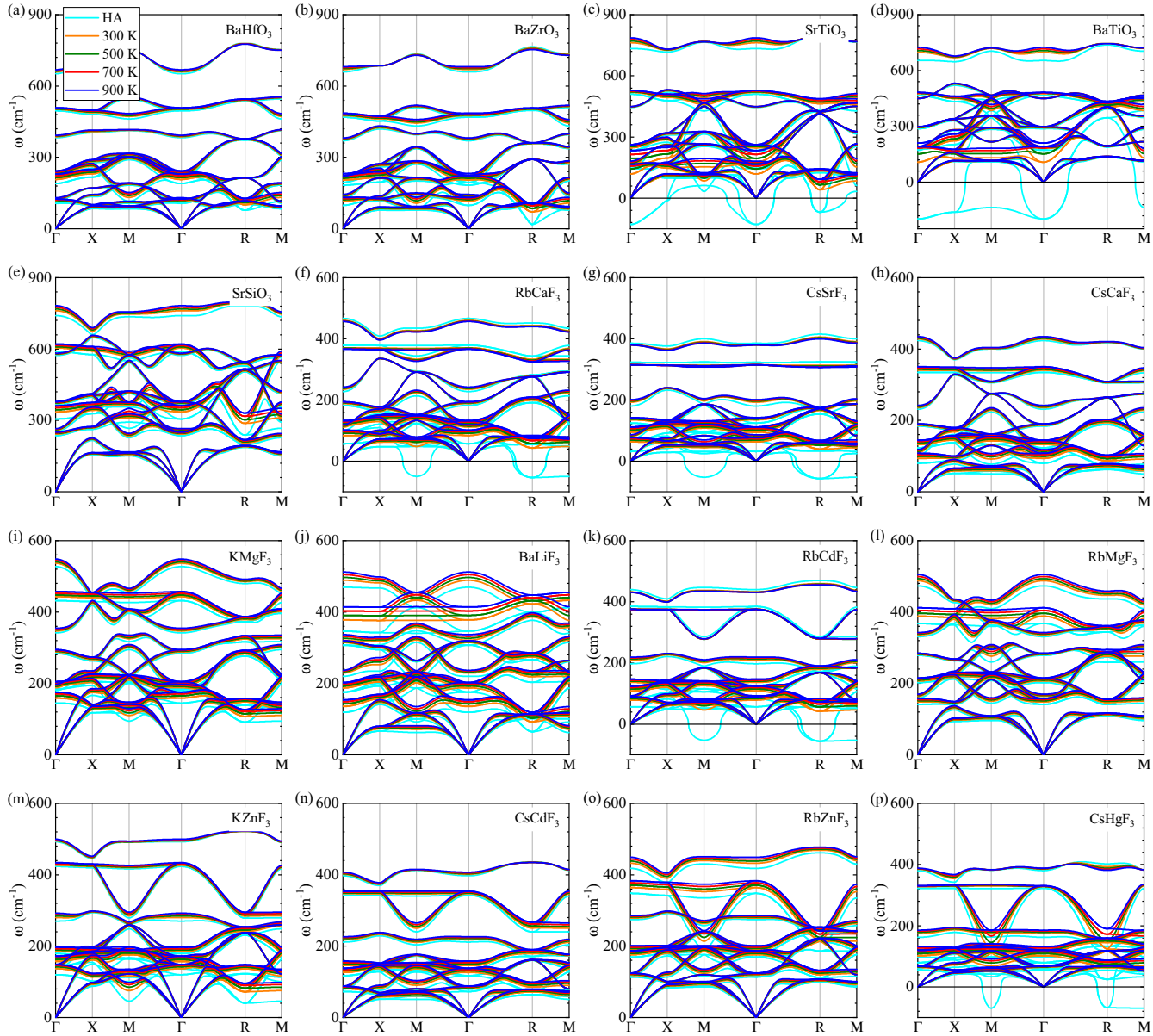

FIG. 9. HA and SCP phonon spectra for 16 cubic perovskites: (a) $BaHfO_3$, (b) $BaZrO_3$, (c) $SrTiO_3$, (d) $BaTiO_3$, (e) $SrSiO_3$, (f) $RbCaF_3$, (g) $CsSrF_3$, (h) $CsCaF_3$, (i) $KMgF_3$, (j) $BaLiF_3$, (k) $RbCdF_3$, (l) $RbMgF_3$, (m) $KZnF_3$, (n) $CsCdF_3$, (o) $RbZnF_3$, and (p) $CsHgF_3$. The cyan line represents the HA dispersion, and the orange, green, red, and blue lines denote the SCP dispersions at 300, 500, 700, and 900 K, respectively.

accumulation keeps increasing with the increase of MFP, until reaching a plateau at the MFP equal to 335 (278) nm for cubic $BaHfO_3$ and 76 (43) nm for cubic $CsSrF_3$. Obviously, the maximum MFP in cubic $BaHfO_3$ is much longer than that in cubic $CsSrF_3$, which is consistent with the higher phonon group velocities $v_{\mathbf{q}\nu}$ in cubic $BaHfO_3$, as shown in Fig. 16. Compared with the results within the SCP + 3ph model, the MFP cumulative κ_L calculated within the SCP + 3, 4ph one shows that 4ph scatterings reduce the maximum MFP from 335 (76) to 278 (43) nm in cubic $BaHfO_3$ ($CsSrF_3$). Meanwhile, the 4ph scatterings strongly suppress the heat transfer of the thermal carriers with the MFP longer than 10 (2.5) nm in cubic $BaHfO_3$ ($CsSrF_3$). More interestingly, the heat transfer performance of the thermal carriers with MFP below 2.5 nm in cubic $CsSrF_3$ is evidently enhanced by the 4ph scatterings, as shown in Fig. 7. Furthermore, phonons with MFP below 100 nm provide about 80% (83%) of the total κ_{3ph}^{SCP} ($\kappa_{3,4ph}^{SCP}$) for cubic $BaHfO_3$. This signifies that creating nanostructuring with the length of 100 nm would reduce the κ_{3ph}^{SCP} ($\kappa_{3,4ph}^{SCP}$) by 20% (17%) in this material. Thus, to significantly reduce the κ_L in cubic $BaHfO_3$, nanostructures with a characteristic length below 100 nm are required.

Now we come back to the anomalous temperature dependence of the κ_L for cubic $RbCaF_3$ in the temperature range from 100 to 300 K shown in Fig. 2(f). According to Eq. (1), the κ_L within SMRTA is determined by constant-volume specific heat $C_v = \sum_{\mathbf{q}\nu} \frac{1}{k_B T^2 \Omega} (\hbar\omega_{\mathbf{q}\nu})^2 n_{\mathbf{q}\nu}(n_{\mathbf{q}\nu}+1)$, squared phonon group velocity $v_{\mathbf{q}\nu}^2$, and lifetime $\tau_{\mathbf{q}\nu}$. Therefore, due to rapidly enhanced C_v, the κ_L is always increasing as temperature increases from 0 K to a value at which the κ_L reaches

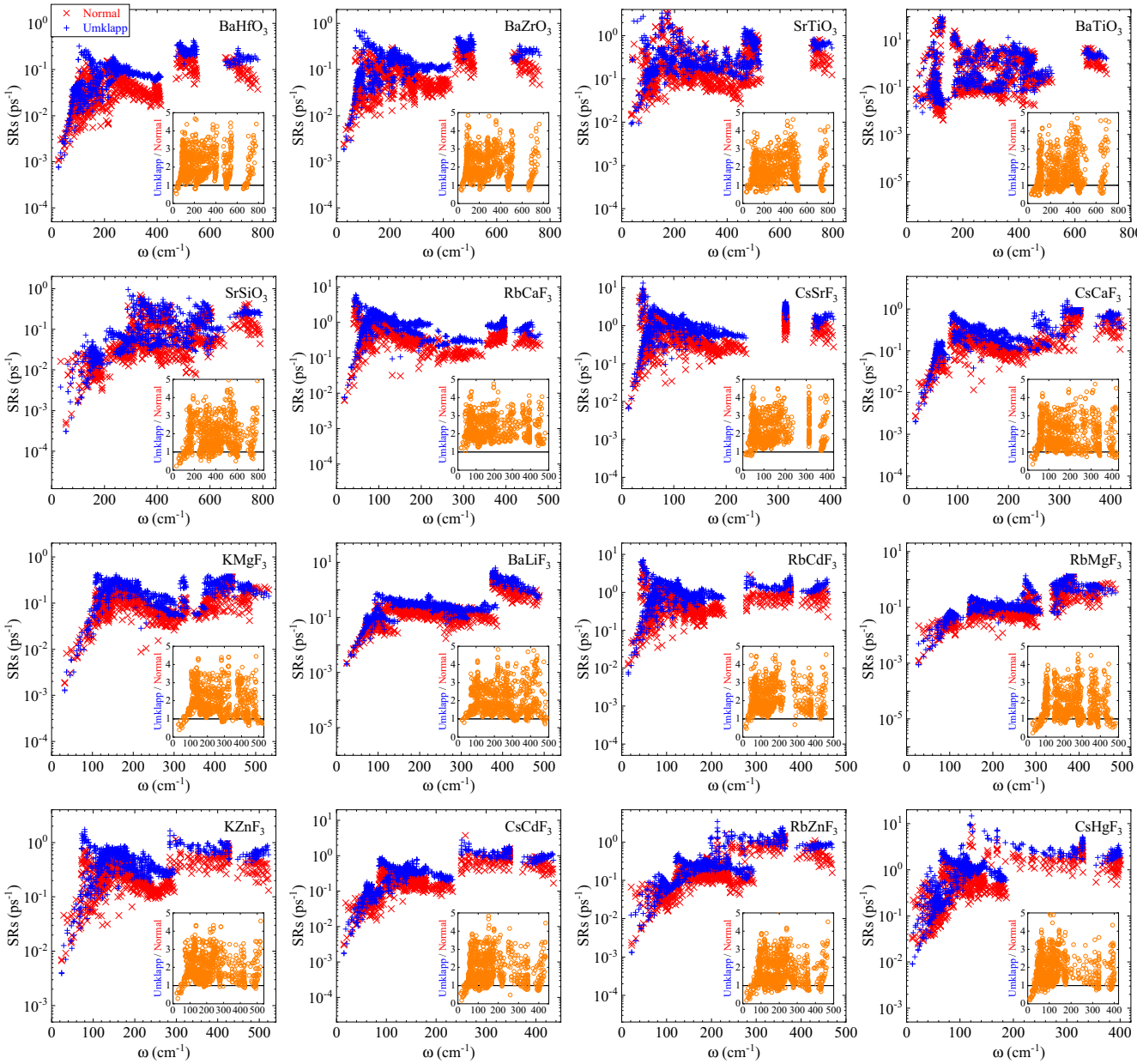

FIG. 10. Decomposed 4ph scatterings into the normal and Umklapp processes for 16 cubic perovskites at 300 K. Insets shows the ratios between Umklapp and normal processes.

a peak, and then the κ_L decreases with rising temperature because of the combined action of the almost constant C_v and enhanced SRs. For the cubic $RbCaF_3$, our results indicate that the peak of κ_L occurs around 300 K, while this peak in other perovskites should be discovered below 100 K under which the κ_L we have not focused on.

To reveal the delayed peak of κ_L as the increasing temperature in cubic $RbCaF_3$, we analyze the differences of C_v and total SRs within the SCP + 3, 4ph model between 100 and 300 K, as shown in Fig. 8. The same information for cubic $CsSrF_3$ and $SrSiO_3$, two candidates with the highest and lowest C_v, respectively (see Fig. 18), are also given for comparison. We observe that the difference of C_v between 100 and 300 K in cubic $RbCaF_3$ is 4.55 meV/nm^{3}K, much larger than the difference of 2.81 meV/nm^{3}K in cubic $CsSrF_3$, as shown in Fig. 8(a), while the differences of total SRs between 100 and 300 K for both materials are similar to each other, as shown in Fig. 8(d). At the same time, the total SRs in cubic $RbCaF_3$ and $CsSrF_3$ are enhanced very slowly from 100 to 300 K, and some SRs below 150 cm^{-1} even have negative enhancements, as demonstrated by the SR ratios lower than 1.0 shown in Fig. 8(d). The slow enhancement of SRs with rising temperature can be ascribed to the presence of strong lattice anharmonicity at the low temperature approaching the phase transition that will break the cubic balance structure. As a result, the competition of quickly increasing C_v and slowly enhanced SRs with rising temperature leads to an ascending κ_L at temperatures below 300 K in cubic $RbCaF_3$, and the combination of weakly increasing C_v with slowly enhanced SRs gives rise to a weakly decreasing κ_L, or say,

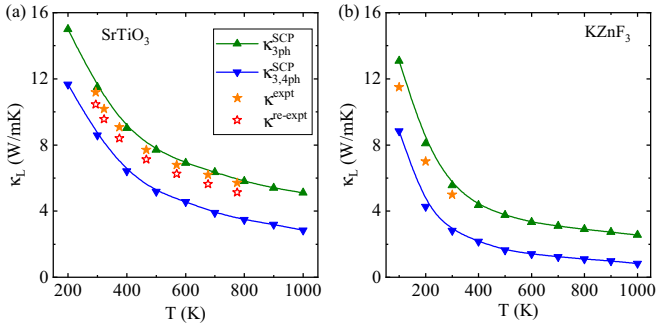

FIG. 11. The κ_{3ph}^{SCP} and $\kappa_{3,4ph}^{SCP}$ calculated within experimental lattice constants for cubic $SrTiO_3$ (a) and $KZnF_3$ (b). The lines and orange pentagram have the same color legend as those in Fig. 2. The red pentagram in (a) is the revised experimental κ_L by excluding electrical thermal conductivity κ_{el}.

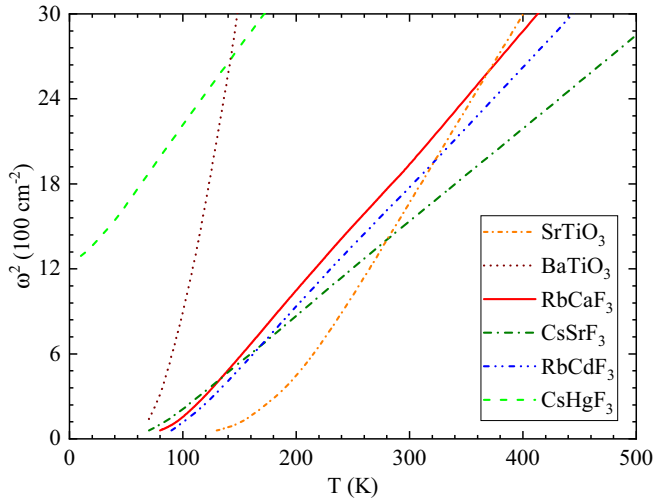

FIG. 12. Temperature dependence of the squared frequencies ω^2 of the softest low-lying mode in cubic $SrTiO_3$, $BaTiO_3$, $RbCaF_3$, $CsSrF_3$, $RbCdF_3$, and $CsHgF_3$.

weak temperature dependence of the κ_L, in cubic $CsSrF_3$. As a counterexample, cubic $SrSiO_3$ has a larger difference of C_v between 100 and 300 K than that in cubic $RbCaF_3$, but its SR is sharply enhanced by the rising temperature, and thus the κ_L in cubic $SrSiO_3$ has a swiftly decreasing trend with increasing temperature.

More precisely, the differences of effective C_v and SRs, that is, the ones that play significant roles in the formation of the κ_L, between different temperatures should be analyzed to reveal the anomalous temperature dependence of κ_L. As examples, we first plot the rescaled cumulative κ_L (the cumulative κ_L divided by the total κ_L) at 100 and 300 K for cubic $RbCaF_3$, $CsSrF_3$, and $SrSiO_3$ to determine the phonons playing crucial roles in forming the κ_L, as shown in Fig. 8(b). One can observe that the κ_L in cubic $RbCaF_3$ ($CsSrF_3$) at both 100 and 300 K are mainly contributed by the phonons with frequency below about 380 (220) cm^{-1}. From the frequency-cumulative specific heat $C_v(\omega)$ plotted in Fig. 8(c), we find that the difference of cumulative $C_v(\omega)$ at 380 cm^{-1} between 100 and 300 K in cubic $RbCaF_3$ is more than twice that at 220 cm^{-1} in cubic $CsSrF_3$, which displays a bigger difference between the changes of effective C_v with increasing temperature in the two materials, and thus becomes more conducive to understanding the different temperature dependence of the κ_L between them. For the cubic $SrSiO_3$, the rescaled cumulative κ_L exhibits that the phonons below 300 (600) cm^{-1} dominate the κ_L at 100 (300) K, and thus the effective C_v at 300 K becomes larger than that at 100 K. However, this does not affect the rapid decline of the κ_L with rising temperature in cubic $SrSiO_3$. As shown in Figs. 8(b) and 8(d), one can see that in cubic $SrSiO_3$ the increasing of temperature from 100 to 300 K not only enhances the total SRs below 300 cm^{-1} sharply but also opens the phonon scatterings between 300 and 600 cm^{-1}, which play negligible roles in formation of the κ_L at 100 K.

Besides the changes of C_v and SRs driven by rising temperature, the differences of squared phonon group velocity $v_{\mathbf{q}\nu}^2$ between 100 and 300 K are also required to analyze the anomalous temperature dependence of the κ_L. Our calculations demonstrate that the rising-temperature-driven differences of $v_{\mathbf{q}\nu}^2$ are considerably small in the considered cubic perovskites, which has a negligible effect on the temperature dependence of the κ_L compared with the rising-temperature-driven changes of C_v and SRs. In other words, in finite-temperature phonon spectra, the shifts of phonon frequencies, which are included in specific heat C_v, play more important roles than those of group velocities in determining the temperature dependence of the κ_L.

Finally, we note that the phonon frequency shifts induced by cubic anharmonicity and quasiharmonic effect are neglected in the present SCP calculations. If these effects are included, the hardening of low-frequency phonons will be slightly restrained, and thus the resulting κ_L may be lowered somewhat. However, the used SMRTA scheme in solution of the BTE to treat 4ph scatterings provides a slightly underestimated κ_L, although the fact that Umklapp processes dominate over the normal ones shows the rationality of the SMRTA scheme. This maybe more or less offsets the influence of neglecting the quasiharmonic effect and the phonon frequency shifts from cubic anharmonicity on the final κ_L. As a prospect, the improved SCP theory [95,96], which can include both quartic and cubic anharmonicities simultaneously in calculations of anharmonic phonons (in other words, consider first- to second-order energy corrections to phonon eigenvalues [27]), and the fully iterative scheme for not only 3ph scatterings but also 4ph processes are recommended to use in future calculations for the κ_L; only this will consume very huge computing resources.

IV. CONCLUSION

In conclusion, we have systematically investigated four different kinds of lattice thermal conductivities κ_{3ph}^{HA}, $\kappa_{3,4ph}^{HA}$, κ_{3ph}^{SCP}, and $\kappa_{3,4ph}^{SCP}$ in 16 of the most common cubic oxide and fluoride perovskites able to exist at room temperature by using a high-throughput first-principles calculation method that combines SCP theory, CS techniques, and phonon BTE. The phonon BTE was solved on top of the SCP theory to completely include the quartic anharmonicity comprising phonon frequency shifts and 4ph scatterings processes. In particular,

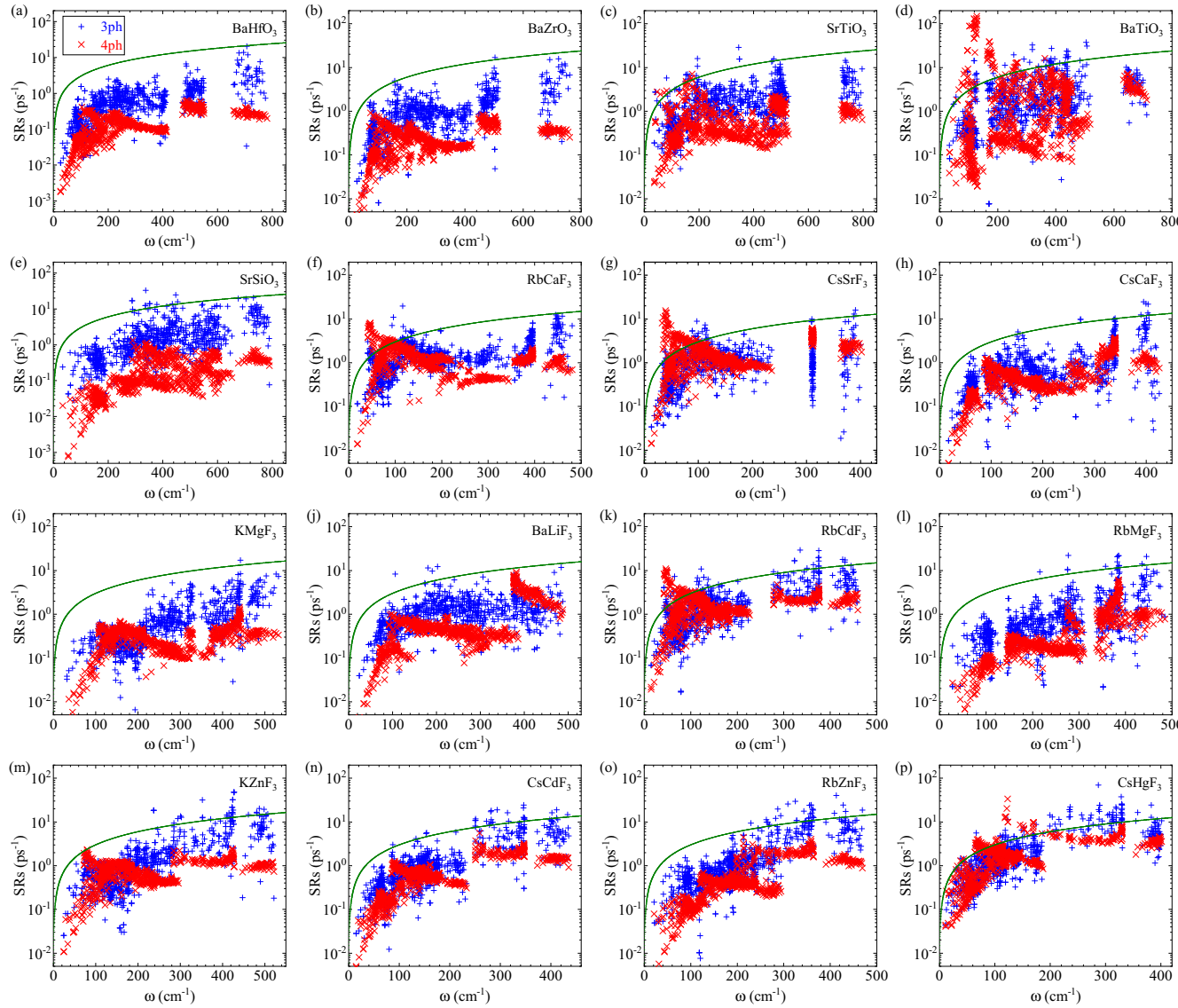

FIG. 13. 3,4ph scatterings at 300 K for 16 cubic perovskites: (a) $BaHfO_3$, (b) $BaZrO_3$, (c) $SrTiO_3$, (d) $BaTiO_3$, (e) $SrSiO_3$, (f) $RbCaF_3$, (g) $CsSrF_3$, (h) $CsCaF_3$, (i) $KMgF_3$, (j) $BaLiF_3$, (k) $RbCdF_3$, (l) $RbMgF_3$, (m) $KZnF_3$, (n) $CsCdF_3$, (o) $RbZnF_3$, and (p) $CsHgF_3$. The green curves indicate the SRs equal to phonon frequencies.

only the κ_L within the SCP theory is numerically valid for six of the 16 candidate perovskites, since the common calculation of BTE within the HA fails to estimate the κ_L due to the presence of imaginary frequencies in these materials. We discovered that in addition to 3ph scattering processes, the complete inclusion of quartic anharmonic effect is indispensable to obtain a rational κ_L and corresponding temperature dependence, while the consideration of only 4ph scattering processes (phonon frequency shifts) tends to produce an underestimated (overestimated) κ_L and stronger (weaker) temperature dependence. At the same time, our calculations gave a roughly linear relation between the $\kappa^{SCP}_{3,4ph}$ and 4ph scatterings in the 16 considered cubic perovskites, which indicates that the structures with lower $\kappa^{SCP}_{3,4ph}$ have stronger 4ph scatterings. Unlike previous works, very strong 4ph scatterings were discovered in some cubic perovskites, especially in the cubic fluoride perovskites with imaginary HA phonons. Through the analyses of thermal conductivity spectrum $\kappa_L(\omega)$, scattering process, phase space, etc., we revealed that cubic $CsSrF_3$, $CsHgF_3$, and $RbCdF_3$, which have anomalously low heat

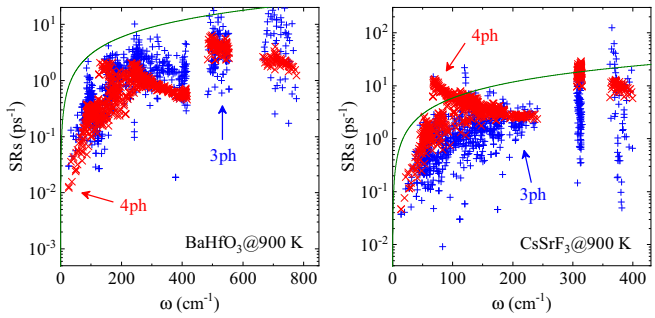

FIG. 14. 3,4ph scatterings at 900 K for cubic $BaHfO_3$ and $CsSrF_3$. The green curves indicate the SRs equal to phonon frequencies.

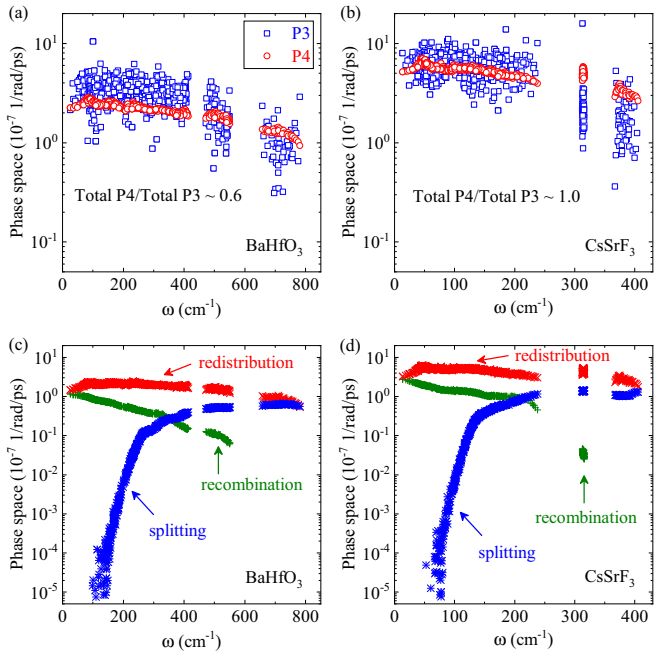

FIG. 15. P_3 and P_4 at 300 K for cubic $BaHfO_3$ (a) and $CsSrF_3$ (b), and decomposed P_4 into the splitting ($\lambda \rightarrow \lambda' + \lambda'' + \lambda'''$), redistribution ($\lambda + \lambda' \rightarrow \lambda'' + \lambda'''$), and recombination ($\lambda + \lambda' + \lambda'' \rightarrow \lambda'''$) processes for cubic $BaHfO_3$ (c) and $CsSrF_3$ (d).

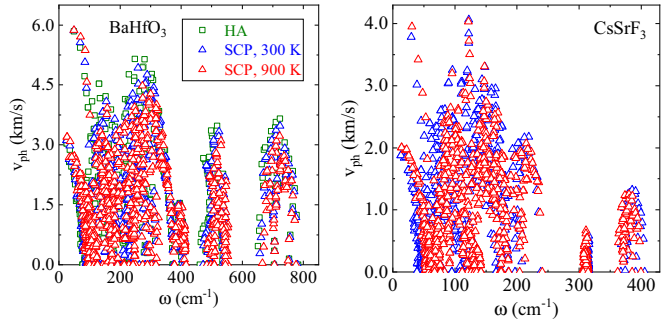

FIG. 16. The phonon group velocities $v_{\mathbf{q}\nu}$ for cubic $BaHfO_3$ and $CsSrF_3$. The HA results for cubic $BaHfO_3$ and the SCP results at 300 and 900 K for both materials are shown.

conduction, e.g., with room-temperature $\kappa_{3,4ph}^{SCP} < 1$ W/mK, possess the scattering strengths of 4ph processes comparable to or even exceeding those of the 3ph ones. In addition, redistribution processes and Umklapp processes dominate the strong 4ph scatterings, which also shortens the maximum MFP and thus changes the heat transfer performance of some thermal carriers with particular MFP. At last, we have discussed the anomalous temperature dependence of the κ_L for cubic $RbCaF_3$ in the temperature range from 100 to 300 K, and found that the competition of quickly increasing effective specific heat $C_v(\omega)$ and slowly enhanced total scatterings with rising temperature leads to an ascending κ_L at temperatures below 300 K. This paper sheds light on the community of studying thermal and thermoelectric transport in perovskite materials.

ACKNOWLEDGMENTS

This research was supported by the National Natural Science Foundation of China under Grants No. 12174327, No. 11974302, No. 11774396, and No. 11774195; and the National Key Research and Development Program of China under Grants No. 2016YFA0300902 and No. 2016YFB0700102.

APPENDIX A: HA AND SCP PHONON SPECTRA AT DIFFERENT TEMPERATURES FOR 16 CUBIC PEROVSKITES

The phonon spectra within the HA and SCP approximation for the 16 considered cubic perovskites are shown in Fig 9. The HA phonon spectra in cubic $BaHfO_3$, $BaZrO_3$, $SrSiO_3$, $CsCaF_3$, $KMgF_3$, $BaLiF_3$, $RbMgF_3$, $KZnF_3$, $CsCdF_3$, and $RbZnF_3$ have no imaginary frequency, which not only supports the dynamical stability of these structures but also means the numerical validness of the solutions of BTE within the HA. However, the low-lying HA modes around the M, R, or Γ points in cubic $SrTiO_3$, $BaTiO_3$, $RbCaF_3$, $CsSrF_3$, $RbCdF_3$, and $CsHgF_3$ are unstable, e.g., with some imaginary frequencies for the softest mode around these points. After considering quartic anharmonic renormalization, the SCP phonon spectra in cubic $SrTiO_3$, $BaTiO_3$, $RbCaF_3$, $CsSrF_3$, $RbCdF_3$, and $CsHgF_3$ become absent of imaginary frequency at each considered temperature because of the large frequency shifts of the low-lying phonon modes in these materials. At the same time, the low-lying modes around the R point in cubic $BaHfO_3$, $BaZrO_3$, $KMgF_3$, $BaLiF_3$, and $KZnF_3$ are also evidently hardened by the quartic anharmonicity. These findings hint that most of the considered perovskites have strong quartic anharmonicity, and thus it is essential to include the 4ph scattering in computing the κ_L of these materials, especially when the SCP phonons are used in calculations of the κ_L. In addition, the high-frequency modes have relatively weak quartic anharmonic renormalization in cubic $BaHfO_3$, $BaZrO_3$, $CsCaF_3$, $KZnF_3$, $CsCdF_3$, and $CsHgF_3$, small positive renormalization to phonons in cubic $SrTiO_3$, $BaTiO_3$, $SrSiO_3$, $KMgF_3$, $BaLiF_3$, $RbMgF_3$, and $RbZnF_3$, and small negative renormalization in cubic $RbCaF_3$, $CsSrF_3$, and $RbCdF_3$.

APPENDIX B: NORMAL AND UMKLAPP SCATTERING PROCESSES AT 300 K FOR 16 CUBIC PEROVSKITES

In calculations of the κ_L, a particular problem we need to consider is whether to solve the BTE exactly with an iterative scheme beyond the SMRTA to gain a converged result of the κ_L. This is closely associated with the relative strength of phonon normal/Umklapp processes [91,92]. If the Umklapp processes dominate over the normal ones, the accuracy of the calculated κ_L without using an iterative scheme can be acceptable. In our present calculations, 4ph processes are treated by the SMRTA scheme, while the iterative method is used to deal with 3ph processes. Therefore, the normal/Umklapp processes of 4ph scatterings should be checked to verify whether the calculated $\kappa_{3,4ph}^{SCP}$ is rational. Moreover, the $\kappa_{3,4ph}^{SCP}$ in cubic $SrTiO_3$ and $KZnF_3$ are lower than the experimental results, as shown in Figs. 2(c) and 2(m). One latent reason is that the

solution of $\kappa_{3,4ph}^{SCP}$ is performed with 4ph scattering processes treated by the SMRTA scheme, which may underestimate the κ_L if the materials have stronger 4ph normal processes [91,92]. For the reasons mentioned above, we provide the normal and Umklapp processes of 4ph scatterings and the corresponding ratios between the Umklapp and normal processes at 300 K for the considered 16 cubic perovskites, as shown in Fig. 10. One can find that the Umklapp processes dominate over the normal ones in all 16 candidate materials, and most of the ratios between Umklapp and normal processes have values above 1.0. These findings demonstrate the reasonableness of application of the SMRTA scheme to treat 4ph scattering processes in the 16 chosen materials. Hence, the inconsistency between $\kappa_{3,4ph}^{SCP}$ and the experimental values in cubic $SrTiO_3$ and $KZnF_3$ should be ascribed to other factors.

APPENDIX C: κ_{3ph}^{SCP} and $\kappa_{3,4ph}^{SCP}$ CALCULATED WITH EXPERIMENTAL LATTICE CONSTANTS FOR CUBIC $SrTiO_3$ and $KZnF_3$

For cubic $SrTiO_3$ and $KZnF_3$, another latent reason for the inconsistency of $\kappa_{3,4ph}^{SCP}$ with experimental results is that the used GGA-PBE functional tends to overestimate the lattice constant, which may also affect the final κ_L. Therefore, we recalculate κ_{3ph}^{SCP} and $\kappa_{3,4ph}^{SCP}$ by using the experimental lattice constants for cubic $SrTiO_3$ and $KZnF_3$, as plotted in Fig. 11. It can be found that the obtained $\kappa_{3,4ph}^{SCP}$ are enhanced some but still lower than the experimental values. Nonetheless, our calculations are analogous to the findings in previous work which shows that the calculated κ_{3ph}^{SCP} agrees with the experimental values in cubic $SrTiO_3$ [27], as shown in Figs. 2(c) and 11(a). Moreover, we also observe that some experimental samples of cubic $SrTiO_3$ have the electrical conductivity σ even approaching 10^5 S/m at 300 K [76], which gives rise to an electrical thermal conductivity $\kappa_{el} \sim 0.732$ W/mK according to the Wiedemann-Franz formula $\kappa_{el} = L\sigma T$. At the same time, we know that the measured total thermal conductivity, which is composed of κ_L and κ_{el}, is usually taken as the κ_L for semiconductors. That is, to estimate the rationality of calculations, the calculated $\kappa_{3,4ph}^{SCP}$ should be compared with the revised experimental κ_L which is obtained from excluding the electrical thermal conductivity κ_{el} in the measured thermal conductivity. As shown in Fig. 11(a), we find that $\kappa_{3,4ph}^{SCP}$ becomes closer to the revised value of κ_L^{expt}, although still somewhat lower than it. In addition, using advanced theory beyond DFT, e.g., DFT + U or hybrid functionals, may further improve the calculated $\kappa_{3,4ph}^{SCP}$, which will be addressed in future work.

APPENDIX D: TEMPERATURE DEPENDENCE OF THE SQUARED FREQUENCIES ω^2 OF THE SOFTEST LOW-LYING MODE IN CUBIC $SrTiO_3$, $BaTiO_3$, $RbCaF_3$, $CsSrF_3$, $RbCdF_3$, AND $CsHgF_3$

As shown in Fig. 9, the SCP phonon spectra have the softest low-lying mode at the Γ point in cubic $BaTiO_3$ and the R point in cubic $SrTiO_3$, $RbCaF_3$, $CsSrF_3$, $RbCdF_3$, and $CsHgF_3$. To reveal a latent phase transition temperature T_{pt} below which the cubic structural phase cannot exist, the variations of squared phonon frequencies ω^2 with temperature T for the softest low-lying mode in cubic $SrTiO_3$, $BaTiO_3$, $RbCaF_3$, $CsSrF_3$, $RbCdF_3$, and $CsHgF_3$ are plotted in Fig. 12. One can find that the curves of ω^2 versus T in the six materials are almost linear at high temperatures. As the temperature decreases, the curves become nonlinear with temperature, especially in cubic $SrTiO_3$, which results from the numerical artifact of the SCP calculations. Therefore, the fitting of the linear region of the curve should be used to predict the T_{pt}. We find from the fitting results that ω^2 tends to zero at $T \sim 180$, 80, 90, 75, and 93 K for the softest low-lying mode in cubic $SrTiO_3$, $BaTiO_3$, $RbCaF_3$, $CsSrF_3$, and $RbCdF_3$, respectively, demonstrating the freezing out of the softest low-lying mode and existence of a latent structural phase transition. For cubic $SrTiO_3$, our $T_{pt} \sim 180$ K is higher than the cubic-to-tetragonal phase transition observed at 105 K in experiments [23,24], but agrees with previous similar calculations [27]. For cubic $CsHgF_3$, there is no freezing out of any soft mode as temperature decreases, meaning that this structure can exist at any low temperatures. Given the fact that $BaTiO_3$ undergoes cubic, tetragonal, orthorhombic, and rhombohedral crystal structures from high to low temperature, we can witness that the application of SCP frequency or its square is not enough to reveal the true phase transition in some cases. For instance, the experimental T_{pt} of cubic-to-tetragonal transition for $BaTiO_3$ is about 400 K [93], which is much higher than the $T_{pt} \sim 80$ K estimated here. Based on the SCP results, we can conclude that the cubic phase of $BaTiO_3$ is able to exist at temperatures above 80 K, only it is a metastable structural phase until the temperature exceeds 400 K.

APPENDIX E: 3, 4ph SCATTERINGS AT 300 K FOR 16 CUBIC PEROVSKITES

To facilitate understanding the differences of the calculated $\kappa_{3,4ph}^{SCP}$ among the selected cubic perovskites and demonstrating more cases with strong 4ph scatterings, the SRs of 3ph and 4ph processes at 300 K for the considered 16 cubic perovskites are shown in Fig. 13. Overall, the candidates with higher $\kappa_{3,4ph}^{SCP}$ have relatively smaller 3ph and 4ph scatterings. More interestingly, one can observe that besides cubic $CsSrF_3$, the 4ph scattering processes in cubic $BaTiO_3$, $RbCaF_3$, $CsCaF_3$, $RbCdF_3$, $KZnF_3$, and $CsHgF_3$ are also comparable to the 3ph ones, which is corresponding to the ratios of $\kappa_{3,4ph}^{SCP}/\kappa_{3ph}^{SCP}$ shown in Fig. 3, in which the values of $\kappa_{3,4ph}^{SCP}/\kappa_{3ph}^{SCP}$ for cubic $BaTiO_3$, $RbCaF_3$, $CsSrF_3$, $CsCaF_3$, $RbCdF_3$, $KZnF_3$, and $CsHgF_3$ are smaller than 0.6. In addition, the majority of 3ph and 4ph scatterings in these materials are distributed below the curves with SRs equal to phonon frequencies, supporting the suitableness of phonon quasiparticle picture.

APPENDIX F: 3, 4ph SCATTERINGS AT 900 K FOR CUBIC $BaHfO_3$ AND $CsSrF_3$

The 3ph and 4ph scatterings at 900 K in cubic $BaHfO_3$ and $CsSrF_3$ are plotted in Fig. 14. On can discover that with increasing temperature, the 4ph scatterings are obviously stronger than the 3ph ones in cubic $CsSrF_3$. At the same time, the 4ph processes in cubic $BaHfO_3$ also become comparable to the 3ph ones. These results signify that the 4ph scatterings

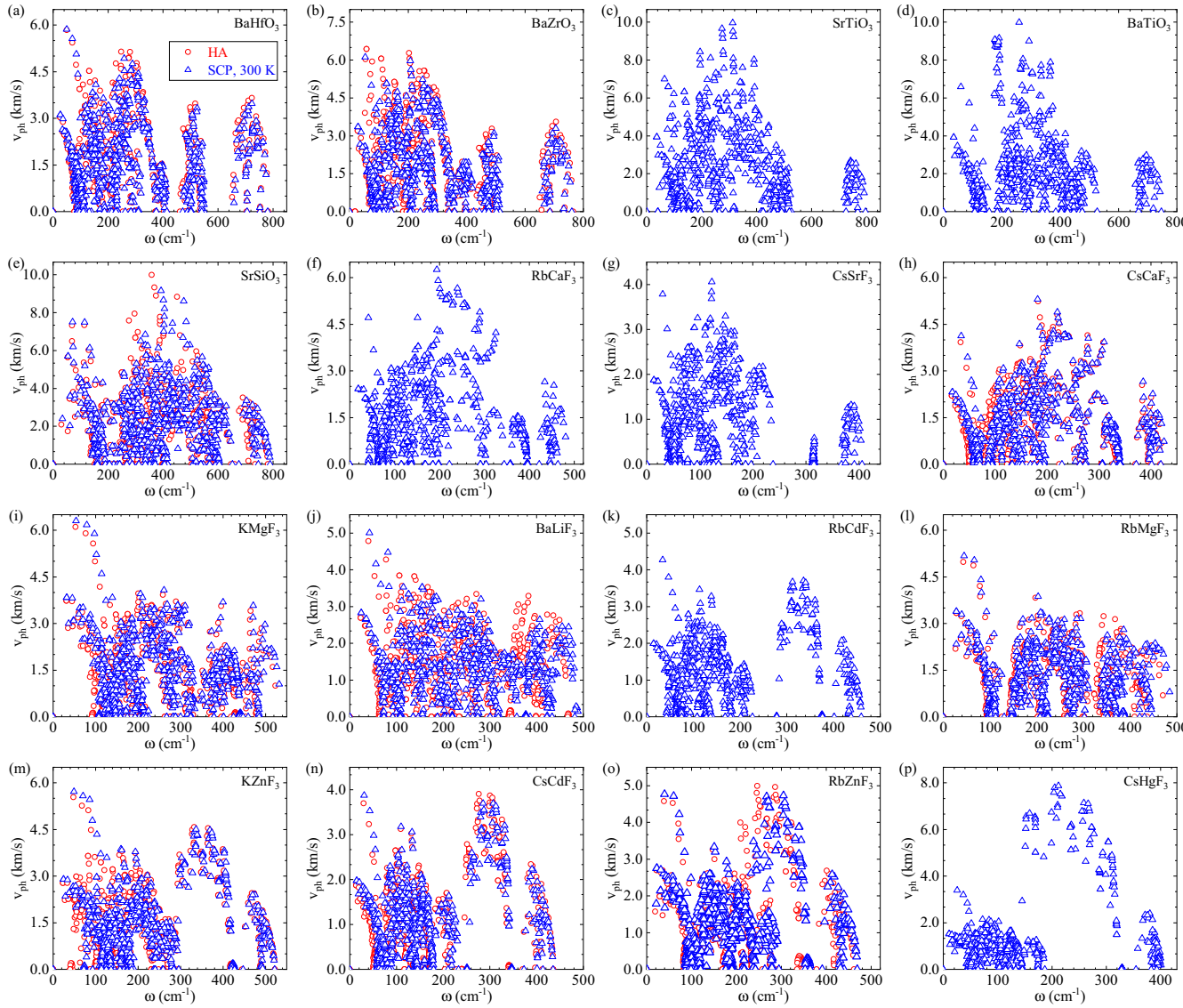

FIG. 17. The SCP phonon group velocities $v_{\mathbf{q}\nu}$ at 300 K for 16 cubic perovskites. For the ten cubic perovskites with stable HA phonons, the HA group velocities $v_{\mathbf{q}\nu}$ are also plotted for comparison.

at high temperatures are stronger than or at least comparable to the 3ph ones, displaying the significance of the inclusion of 4ph scatterings in calculations of the κ_L. Moreover, even if the 3ph and 4ph scatterings are strengthened by the enhanced temperature, the majority of them are still distributed below the curves with SRs equal to phonon frequencies and, consequently, the phonon quasiparticle picture maintains validity.

APPENDIX G: 3, 4ph SCATTERING PHASE SPACE AND DECOMPOSED 4ph SCATTERING PHASE SPACE FOR CUBIC $BaHfO_3$ AND $CsSrF_3$

The 3ph and 4ph scattering phase spaces (P_3 and P_4) at 300 K for cubic $BaHfO_3$ and $CsSrF_3$ are shown in Figs. 15(a) and 15(b), which indicates that the total P_4 in cubic $CsSrF_3$ are almost the same as the total P_3, while the total P_4 are relatively lower than the total P_3 in cubic $BaHfO_3$. This interprets the relatively stronger 4ph scatterings in cubic $CsSrF_3$. The 4ph phase spaces are also decomposed into those arising from three individual processes, namely, splitting ($\lambda \rightarrow \lambda' + \lambda'' + \lambda'''$), redistribution ($\lambda + \lambda' \rightarrow \lambda'' + \lambda'''$), and recombination ($\lambda + \lambda' + \lambda'' \rightarrow \lambda'''$) processes, respectively, as shown in Figs. 15(c) and 15(d). Considering the constraint imposed by the conservation of phonon energies in scattering processes, it is expected that the splitting processes are largely associated with the high-lying phonon modes while the recombination processes are more related to phonons with low frequencies. On the other hand, the redistribution processes are more flexible in satisfying the conservation of phonon energies, thus contributing many more 4ph scattering events [94]. Hence, both 4ph phase spaces and 4ph scatterings are dominated by the redistribution processes, as shown in Figs. 6(a), 6(c), 15(c), and 15(d). At the same time, low-frequency and high-frequency phonons have considerable recombination and splitting processes, respectively, as shown in Figs. 15(c) and 15(d), which is consistent with the constraint enforced by energy conservation.

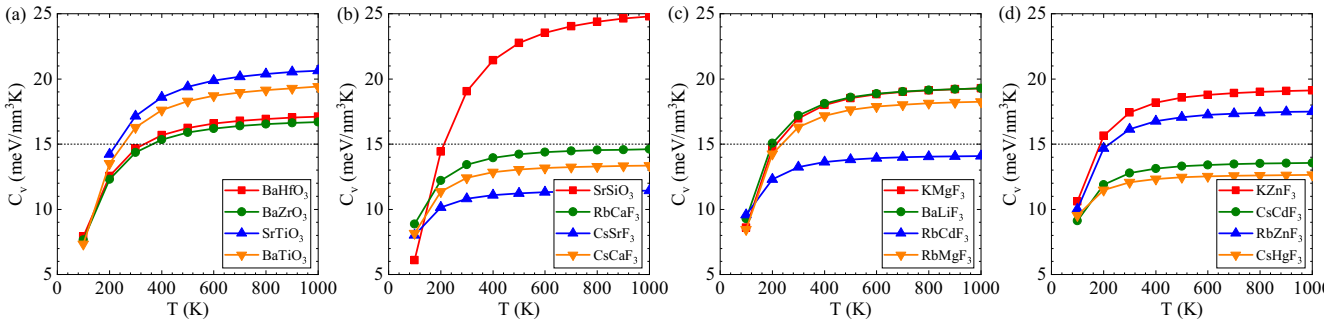

FIG. 18. Constant-volume specific heat C_v for 16 cubic perovskites. The cubic $RbCaF_3$, $CsSrF_3$, $CsCaF_3$, $RbCdF_3$, $CsCdF_3$, and $CsHgF_3$ have relatively smaller C_v, as divided by the dashed lines.

APPENDIX H: HA AND SCP PHONON GROUP VELOCITY FOR 16 CUBIC PEROVSKITES

In determination of the origin of the κ_L, the phonon group velocity $v_{\mathbf{q}\nu}$ is another commonly used physical quantity to analyze. To reveal the differences of the calculated $\kappa^{SCP}_{3,4ph}$ between cubic $BaHfO_3$ and $CsSrF_3$, here we first plot the phonon group velocities $v_{\mathbf{q}\nu}$ versus frequencies $\omega_{\mathbf{q}\nu}$ for the two materials in Fig. 16, in which the HA results for cubic $BaHfO_3$ and the SCP results at 300 and 900 K for cubic $BaHfO_3$ and $CsSrF_3$ are shown. From this information, we can find that the quartic anharmonic renormalization mainly affects the phonon frequencies $\omega_{\mathbf{q}\nu}$ which should be ascribed to the constant-volume specific heat C_v, while the group velocities $v_{\mathbf{q}\nu}$ are enhanced very slightly in the phonon frequency range governing the κ_L.

Then the HA phonon group velocity and SCP phonon group velocity at 300 K for the 16 cubic perovskites are shown in Fig. 17 to understand the differences of the κ_L in the selected candidates. From the results in the ten cubic perovskites with stable HA phonons, one can further find that the inclusion of quartic anharmonic renormalization mainly affects the phonon frequencies $\omega_{\mathbf{q}\nu}$ while the group velocities $v_{\mathbf{q}\nu}$ change slightly. In addition, besides the strong 3ph and 4ph scatterings, the candidates with very small κ_L, e.g., $\kappa^{SCP}_{3,4ph} < 2.0$ W/mK, have relatively smaller $v_{\mathbf{q}\nu}$ for the low-frequency phonons, as shown in cubic $CsSrF_3$, $RbCdF_3$, $CsCdF_3$, and $CsHgF_3$ in Fig. 17.

APPENDIX I: CONSTANT-VOLUME SPECIFIC HEAT C_v FOR 16 CUBIC PEROVSKITES

According to Eq. (1), we know that besides the phonon group velocity $v_{\mathbf{q}\nu}$, and total SRs, the constant-volume specific heat C_v is the third physical quantity to determine the results of κ_L. The C_v for the 16 cubic perovskites are plotted in Fig. 18. It can be seen that the cubic $SrSiO_3$ has the largest C_v at high temperatures, while the cubic $CsSrF_3$ possesses the smallest one. Overall, the C_v for the six cubic perovskites $RbCaF_3$, $CsSrF_3$, $CsCaF_3$, $RbCdF_3$, $CsCdF_3$, and $CsHgF_3$ are relatively smaller than those in other cubic perovskites, as divided by the dashed line in Fig. 18, which results from the fact that the majority of phonon branches in the six cubic perovskites have relatively lower frequencies. Through the comprehensive comparisons of C_v, $v_{\mathbf{q}\nu}$, and SRs among different candidates at different temperatures, the origin of the κ_L and its temperature dependence can be analyzed, as narrated in the main text for the anomalous temperature dependence of the κ_L below 300 K in cubic $RbCaF_3$, where the effective $C_v(\omega)$ is also used for more precisely comparisons.

APPENDIX J: TEST FOR THE IFCs CALCULATED WITH THE LAGER SUPERCELL AND SPIN-ORBIT COUPLING

The needed harmonic and anharmonic IFCs are calculated within a $2 \times 2 \times 2$ supercell in this paper. To check whether this supercell is large enough to capture all the primary interatomic interactions, the IFCs within a larger supercell beyond the $2 \times 2 \times 2$ one are calculated for cubic $BaHfO_3$ as an example. The HA phonon dispersions calculated from the harmonic IFCs produced within the $2 \times 2 \times 2$ and $3 \times 3 \times 3$ supercells are plotted in Fig. 19(a). It can be found that the results agree well with each other, signifying that the harmonic IFCs produced within a $2 \times 2 \times 2$ supercell are sufficient to generate the convergent phonons. We can infer that the produced anharmonic IFCs within a $2 \times 2 \times 2$ supercell are also convergent, since the anharmonic IFCs converge more rapidly than the harmonic ones in general.

In addition, the spin-orbit coupling (SOC) is also excluded in our calculations. The cubic $CsHgF_3$, which has strong SOC due to the existence of Hg atom, is taken as an example to verify the feasibility of excluding SOC in present

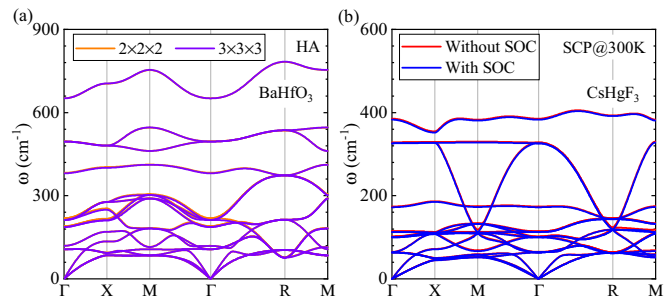

FIG. 19. (a) The HA phonon spectra calculated with the harmonic IFCs produced within the $2 \times 2 \times 2$ and $3 \times 3 \times 3$ supercells for cubic $BaHfO_3$. (b) The SCP phonon spectra at 300 K calculated with and without SOC for cubic $CsHgF_3$.

calculations. As shown in Fig. 19(b), the SCP phonon dispersion at 300 K calculated with SOC is in accordance with the result calculated without SOC, which demonstrates the rationality of exclusion of SOC here.

[1] L. E. Bell, Cooling, heating, generating power, and recovering waste heat with thermoelectric systems, Science **321**, 1457 (2008).

[2] A. Mills, *Heat and Mass Transfer, Irwin Graphics Series* (Taylor & Francis, London, 1995).

[3] R. R. Heikes and R. W. Ure, *Thermoelectricity: Science and Engineering* (Interscience, New York, 1961).

[4] S. L. Shindé and J. Goela, *High Thermal Conductivity Materials* (Springer, New York, 2006).

[5] R. Venkatasubramanian, E. Siivola, T. Colpitts, and B. O'Quinn, Thin-film thermoelectric devices with high room-temperature figures of merit, Nature (London) **413**, 597 (2001).

[6] J. P. Heremans, V. Jovovic, E. S. Toberer, A. Saramat, K. Kurosaki, A. Charoenphakdee, S. Yamanaka, and G. J. Snyder, Enhancement of thermoelectric efficiency in PbTe by distortion of the electronic density of states, Science **321**, 554 (2008).

[7] Y. Pei, A. LaLonde, S. Iwanaga, and G. J. Snyder, High thermoelectric figure of merit in heavy hole dominated PbTe, Energy Environ. Sci. **4**, 2085 (2011).

[8] Y. Pei, X. Shi, A. LaLonde, H. Wang, L. Chen, and G. J. Snyder, Convergence of electronic bands for high performance bulk thermoelectrics, Nature (London) **473**, 66 (2011).

[9] K. Biswas, J. He, I. D. Blum, C.-I. Wu, T. P. Hogan, D. N. Seidman, V. P. Dravid, and M. G. Kanatzidis, High-performance bulk thermoelectrics with all-scale hierarchical architectures, Nature (London) **489**, 414 (2012).

[10] L.-D. Zhao, S.-H. Lo, Y. Zhang, H. Sun, G. Tan, C. Uher, C. Wolverton, V. P. Dravid, and M. G. Kanatzidis, Ultralow thermal conductivity and high thermoelectric figure of merit in SnSe crystals, Nature (London) **508**, 373 (2014).

[11] J. He and T. M. Tritt, Advances in thermoelectric materials research: Looking back and moving forward, Science **357**, eaak9997 (2017).

[12] J. He, M. Amsler, Y. Xia, S. S. Naghavi, V. I. Hegde, S. Hao, S. Goedecker, V. Ozoliņš, and C. Wolverton, Ultralow Thermal Conductivity in Full Heusler Semiconductors, Phys. Rev. Lett. **117**, 046602 (2016).

[13] J. Carrete, W. Li, N. Mingo, S. Wang, and S. Curtarolo, Finding Unprecedentedly Low-Thermal-Conductivity Half-Heusler Semiconductors via High-Throughput Materials Modeling, Phys. Rev. X **4**, 011019 (2014).

[14] L. Xie, J. H. Feng, R. Li, and J. Q. He, First-Principles Study of Anharmonic Lattice Dynamics in Low Thermal Conductivity $AgCrSe_2$: Evidence for a Large Resonant Four-Phonon Scattering, Phys. Rev. Lett. **125**, 245901 (2020).

[15] T. Wu and P. Gao, Development of perovskite-type materials for thermoelectric application, Materials **11**, 999 (2018).

[16] H. Wang, W. Su, J. Liu, and C. Wang, Recent development of n-type perovskite thermoelectrics, J. Materiomics **2**, 225 (2016).

[17] Y. Zhao, C. Lian, S. Zeng, Z. Dai, S. Meng, and J. Ni, Anomalous electronic and thermoelectric transport properties in cubic Rb_3AuO antiperovskite, Phys. Rev. B **102**, 094314 (2020).

[18] Y. Zhao, C. Lian, S. Zeng, Z. Dai, S. Meng, and J. Ni, Quartic anharmonicity and anomalous thermal conductivity in cubic antiperovskites $A_3BO(A = \mathrm{K, Rb}; B = \mathrm{Br, Au})$, Phys. Rev. B **101**, 184303 (2020).

[19] M. Sajjad, Q. Mahmood, N. Singh, and J. A. Larsson, Ultralow lattice thermal conductivity in double perovskite Cs_2PtI_6: A promising thermoelectric material, ACS Appl. Energy Mater. **3**, 11293 (2020).

[20] F. Qian, M. Hu, J. Gong, C. Ge, Y. Zhou, J. Guo, M. Chen, Z. Ge, N. P. Padture, Y. Zhou *et al.*, Enhanced thermoelectric performance in lead-free inorganic $CsSn_{1-x}Ge_xI_3$ perovskite semiconductors, J. Phys. Chem. C **124**, 11749 (2020).

[21] T. Liu, X. Zhao, J. Li, Z. Liu, F. Liscio, S. Milita, B. C. Schroeder, and O. Fenwick, Enhanced control of self-doping in halide perovskites for improved thermoelectric performance, Nat. Commun. **10**, 5750 (2019).

[22] U.-G. Jong, C.-J. Yu, Y.-H. Kye, S.-N. Hong, and H.-G. Kim, Manifestation of the thermoelectric properties in Ge-based halide perovskites, Phys. Rev. Mater. **4**, 075403 (2020).

[23] G. Shirane and Y. Yamada, Lattice-dynamical study of the 110K phase transition in $SrTiO_3$, Phys. Rev. **177**, 858 (1969).

[24] R. A. Cowley, Lattice dynamics and phase transitions of strontium titanate, Phys. Rev. **134**, A981 (1964).

[25] W. Zhong and D. Vanderbilt, Competing Structural Instabilities in Cubic Perovskites, Phys. Rev. Lett. **74**, 2587 (1995).

[26] Z. Xu, Y. Zhao, J. Zhang, K. Chen, C. J. Brabec, and Y. Feng, Phase diagram and stability of mixed-cation lead iodide perovskites: A theory and experiment combined study, Phys. Rev. Mater. **4**, 095401 (2020).

[27] T. Tadano and S. Tsuneyuki, Self-consistent phonon calculations of lattice dynamical properties in cubic $SrTiO_3$ with first-principles anharmonic force constants, Phys. Rev. B **92**, 054301 (2015).

[28] J.-J. Zhou, O. Hellman, and M. Bernardi, Electron-Phonon Scattering in the Presence of Soft Modes and Electron Mobility in $SrTiO_3$ Perovskite from First Principles, Phys. Rev. Lett. **121**, 226603 (2018).

[29] O. Hellman, I. A. Abrikosov, and S. I. Simak, Lattice dynamics of anharmonic solids from first principles, Phys. Rev. B **84**, 180301(R) (2011).

[30] O. Hellman and I. A. Abrikosov, Temperature-dependent effective third-order interatomic force constants from first principles, Phys. Rev. B **88**, 144301 (2013).

[31] P. Souvatzis, O. Eriksson, M. I. Katsnelson, and S. P. Rudin, Entropy Driven Stabilization of Energetically Unstable Crystal Structures Explained from First Principles Theory, Phys. Rev. Lett. **100**, 095901 (2008).

[32] I. Errea, M. Calandra, and F. Mauri, First-Principles Theory of Anharmonicity and the Inverse Isotope Effect in Superconducting Palladium-Hydride Compounds, Phys. Rev. Lett. **111**, 177002 (2013).

[33] N. R. Werthamer, Self-consistent phonon formulation of anharmonic lattice dynamics, Phys. Rev. B **1**, 572 (1970).

[34] T. Tadano, Y. Gohda, and S. Tsuneyuki, Anharmonic force constants extracted from first-principles molecular dynamics: applications to heat transfer simulations, J. Phys.: Condens. Matter **26**, 225402 (2014).

[35] F. Zhou, W. Nielson, Y. Xia, and V. Ozoliņš, Lattice Anharmonicity and Thermal Conductivity from Compressive Sensing of First-Principles Calculations, Phys. Rev. Lett. **113**, 185501 (2014).

[36] F. Zhou, W. Nielson, Y. Xia, and V. Ozoliņš, Compressive sensing lattice dynamics. I. General formalism, Phys. Rev. B **100**, 184308 (2019).

[37] F. Zhou, B. Sadigh, D. Åberg, Y. Xia, and V. Ozoliņš, Compressive sensing lattice dynamics. II. Efficient phonon calculations and long-range interactions, Phys. Rev. B **100**, 184309 (2019).

[38] T. Tadano and S. Tsuneyuki, Quartic Anharmonicity of Rattlers and its Effect on Lattice Thermal Conductivity of Clathrates from First Principles, Phys. Rev. Lett. **120**, 105901 (2018).

[39] Y. Xia, V. I. Hegde, K. Pal, X. Hua, D. Gaines, S. Patel, J. He, M. Aykol, and C. Wolverton, High-Throughput Study of Lattice Thermal Conductivity in Binary Rocksalt and Zinc Blende Compounds Including Higher-Order Anharmonicity, Phys. Rev. X **10**, 041029 (2020).

[40] L. Lindsay, D. A. Broido, and T. L. Reinecke, First-Principles Determination of Ultrahigh Thermal Conductivity of Boron Arsenide: A Competitor for Diamond? Phys. Rev. Lett. **111**, 025901 (2013).

[41] A. Cepellotti, G. Fugallo, L. Paulatto, M. Lazzeri, F. Mauri, and N. Marzari, Phonon hydrodynamics in two-dimensional materials, Nat. Commun. **6**, 6400 (2015).

[42] W. Li and N. Mingo, Ultralow lattice thermal conductivity of the fully filled skutterudite $YbFe_4Sb_{12}$ due to the flat avoided-crossing filler modes, Phys. Rev. B **91**, 144304 (2015).

[43] T. Tadano, Y. Gohda, and S. Tsuneyuki, Impact of Rattlers on Thermal Conductivity Of a Thermoelectric Clathrate: A First-Principles Study, Phys. Rev. Lett. **114**, 095501 (2015).

[44] U. Aseginolaza, R. Bianco, L. Monacelli, L. Paulatto, M. Calandra, F. Mauri, A. Bergara, and I. Errea, Phonon Collapse and Second-Order Phase Transition in Thermoelectric SnSe, Phys. Rev. Lett. **122**, 075901 (2019).

[45] Y. Zhao, Z. Dai, C. Zhang, C. Lian, S. Zeng, G. Li, S. Meng, and J. Ni, High thermopower and potential thermoelectric properties of crystalline LiH and NaH, Phys. Rev. B **95**, 014307 (2017).

[46] Y. Zhao, Z. Dai, C. Lian, S. Zeng, G. Li, J. Ni, and S. Meng, Low lattice thermal conductivity and good thermoelectric performance of cinnabar, Phys. Rev. Mater. **1**, 065401 (2017).

[47] Q. Zheng, C. A. Polanco, M.-H. Du, L. R. Lindsay, M. Chi, J. Yan, and B. C. Sales, Antisite Pairs Suppress the Thermal Conductivity of BAs, Phys. Rev. Lett. **121**, 105901 (2018).

[48] B. Lv, Y. Lan, X. Wang, Q. Zhang, Y. Hu, A. J. Jacobson, D. Broido, G. Chen, Z. Ren, and C.-W. Chu, Experimental study of the proposed super-thermal-conductor: BAs, Appl. Phys. Lett. **106**, 074105 (2015).

[49] J. Kim, D. A. Evans, D. P. Sellan, O. M. Williams, E. Ou, A. H. Cowley, and L. Shi, Thermal and thermoelectric transport measurements of an individual boron arsenide microstructure, Appl. Phys. Lett. **108**, 201905 (2016).

[50] T. Feng, L. Lindsay, and X. Ruan, Four-phonon scattering significantly reduces intrinsic thermal conductivity of solids, Phys. Rev. B **96**, 161201(R) (2017).

[51] A. A. Maradudin and A. E. Fein, Scattering of neutrons by an anharmonic crystal, Phys. Rev. **128**, 2589 (1962).

[52] R. E. Peierls, *Quantum Theory of Solids, International Series of Monographs on Physics* (Clarendon, Oxford, 1996).

[53] A. Debernardi, S. Baroni, and E. Molinari, Anharmonic Phonon Lifetimes in Semiconductors from Density-Functional Perturbation Theory, Phys. Rev. Lett. **75**, 1819 (1995).

[54] W. Li, J. Carrete, N. A. Katcho, and N. Mingo, ShengBTE: A solver of the Boltzmann transport equation for phonons, Comput. Phys. Commun. **185**, 1747 (2014).

[55] Z. Han, X. Yang, W. Li, T. Feng, and X. Ruan, FourPhonon: An extension module to ShengBTE for computing four-phonon scattering rates and thermal conductivity, Comput. Phys. Commun. **270**, 108179 (2022).

[56] P. Hohenberg and W. Kohn, Inhomogeneous electron gas, Phys. Rev. **136**, B864 (1964).

[57] S. Baroni, S. de Gironcoli, A. Dal Corso, and P. Giannozzi, Phonons and related crystal properties from density-functional perturbation theory, Rev. Mod. Phys. **73**, 515 (2001).

[58] G. Kresse and J. Furthmüller, Efficient iterative schemes for ab initio total-energy calculations using a plane-wave basis set, Phys. Rev. B **54**, 11169 (1996).

[59] G. Kresse and J. Furthmüller, Efficiency of ab-initio total energy calculations for metals and semiconductors using a plane-wave basis set, Comput. Mater. Sci. **6**, 15 (1996).

[60] G. Kresse and D. Joubert, From ultrasoft pseudopotentials to the projector augmented-wave method, Phys. Rev. B **59**, 1758 (1999).

[61] J. P. Perdew, K. Burke, and M. Ernzerhof, Generalized Gradient Approximation Made Simple, Phys. Rev. Lett. **77**, 3865 (1996).

[62] T. Maekawa, K. Kurosaki, and S. Yamanaka, Thermal and mechanical properties of perovskite-type barium hafnate, J. Alloys Compd. **407**, 44 (2006).

[63] S. Yamanaka, T. Hamaguchi, T. Oyama, T. Matsuda, S. ichi Kobayashi, and K. Kurosaki, Heat capacities and thermal conductivities of perovskite type $BaZrO_3$ and $BaCeO_3$, J. Alloys Compd. **359**, 1 (2003).

[64] A. Okazaki and M. Kawaminami, Lattice constant of strontium titanate at low temperatures, Mater. Res. Bull. **8**, 545 (1973).

[65] L. Jiang, J. Guo, H. Liu, M. Zhu, X. Zhou, P. Wu, and C. Li, Prediction of lattice constant in cubic perovskites, J. Phys. Chem. Solids **67**, 1531 (2006).

[66] W. Xiao, D. Tan, W. Zhou, J. Liu, and J. Xu, Cubic perovskite polymorph of strontium metasilicate at high pressures, Am. Mineral. **98**, 2096 (2013).

[67] C. Ridou, M. Rousseau, and F. Gervais, The temperature dependence of the infrared reflection spectra in the fluoperovskites $RbCaF_3$, $CsCaF_3$ and $KZnF_3$, J. Phys. C: Solid State Phys. **19**, 5757 (1986).

[68] I. G. Wood, K. S. Knight, G. D. Price, and J. A. Stuart, Thermal expansion and atomic displacement parameters of cubic $KMgF_3$ perovskite determined by high-resolution neutron powder diffraction, J. Appl. Crystallog. **35**, 291 (2002).

[69] A. Boumriche, J. Gesland, A. Bulou, M. Rousseau, J. Fourquet, and B. Hennion, Structure and dynamics of the inverted perovskite $BaLiF_3$, Solid State Commun. **91**, 125 (1994).

[70] M. Rousseau, J. Y. Gesland, J. Julliard, J. Nouet, J. Zarembowitch, and A. Zarembowitch, Crystallographic, elastic, and Raman scattering investigations of structural phase transitions in $RbCdF_3$ and $TlCdF_3$, Phys. Rev. B **12**, 1579 (1975).

[71] A. Raja, G. Annadurai, D. J. Daniel, and P. Ramasamy, Synthesis, structural and optical properties of Eu^{3+} activated fluoroperovskite $RbMgF_3$ phosphors, J. Alloys Compd. **727**, 215 (2017).

[72] K. Knox, Perovskite-like fluorides. I. Structures of $KMnF_3$, $KFeF_3$, $KNiF_3$ and $KZnF_3$. Crystal field effects in the series and in $KCrF_3$ and $KCuF_3$, Acta Crystallog. **14**, 583 (1961).

[73] J.-M. Dance, N. Kerkouri, and A. Tressaud, Evolution structurale par substitution cationique dans les perovskites hexagonales fluorees: II-Les systèmes $Cs_{1-x}Rb_xMF_3$ (M = Mg, Co, Ni, Zn), Mater. Res. Bull. **14**, 869 (1979).

[74] T. Feng and X. Ruan, Quantum mechanical prediction of four-phonon scattering rates and reduced thermal conductivity of solids, Phys. Rev. B **93**, 045202 (2016).

[75] Y. Yuan, X. Zhang, L. Liu, X. Jiang, J. Lv, Z. Li, and Z. Zou, Synthesis and photocatalytic characterization of a new photocatalyst $BaZrO_3$, Int. J. Hydrogen Energ. **33**, 5941 (2008).

[76] H. Muta, K. Kurosaki, and S. Yamanaka, Thermoelectric properties of reduced and La-doped single-crystalline $SrTiO_3$, J. Alloys Compd. **392**, 306 (2005).

[77] S. R. Popuri, A. J. M. Scott, R. A. Downie, M. A. Hall, E. Suard, R. Decourt, M. Pollet, and J.-W. G. Bos, Glass-like thermal conductivity in $SrTiO_3$ thermoelectrics induced by A-site vacancies, RSC Adv. **4**, 33720 (2014).

[78] M. Tachibana, T. Kolodiazhnyi, and E. Takayama-Muromachi, Thermal conductivity of perovskite ferroelectrics, Appl. Phys. Lett. **93**, 092902 (2008).

[79] J. Martin, in *Phonon Scattering in Solids*, edited by L. Challis, V. Rampton, and A. Wyatt (Springer, New York, 1976), pp. 258–260.

[80] W. Pies and A. Weiss, *in KeyElements: F, Cl, Br, I* (Springer-Verlag, Berlin, 1973), pp. 104–115.

[81] M. Rousseau, J. Gesland, B. Hennion, G. Heger, and B. Renker, Low energy phonon dispersion curves of $KZnF_3$ and $CsCaF_3$, Solid State Commun. **38**, 45 (1981).

[82] M. Duarte, M. Vieira, and S. Baldochi, Thermal diffusivity of $BaLiF_3$ crystals, Mater. Sci. Eng. B **25**, 133 (1994).

[83] M. Mortier, J. Gesland, and M. Rousseau, Experimental and theoretical study of second-order raman scattering in $BaLiF_3$, Solid State Commun. **89**, 369 (1994).

[84] M. Shafer and T. McGuire, Preparation and properties of ferrimagnets in the $RbMgF_3$-$RbCoF_3$ system, J. Phys. Chem. Solids **30**, 1989 (1969).

[85] Y. Suemune and H. Ikawa, Thermal conductivity of $KMnF_3$, $KCoF_3$, $KNiF_3$, and $KZnF_3$ single crystals, J. Phys. Soc. Jpn. **19**, 1686 (1964).

[86] P. Daniel, J. Toulouse, J. Y. Gesland, and M. Rousseau, Raman-scattering investigation of the hexagonal perovskite $RbZnF_3$, Phys. Rev. B **52**, 9129 (1995).

[87] R. Hoppe and R. Homann, Über $CsHgF_3$, $RbHgF_3$ und $KHgF_3$, Z. Anorg. Allg. Chem. **369**, 212 (1969).

[88] C. Lasota, C.-Z. Wang, R. Yu, and H. Krakauer, Ab initio linear response study of $SrTiO_3$, Ferroelectrics **194**, 109 (1997).

[89] Z. Tian, J. Garg, K. Esfarjani, T. Shiga, J. Shiomi, and G. Chen, Phonon conduction in PbSe, PbTe, and $PbTe_{1-x}Se_x$ from first-principles calculations, Phys. Rev. B **85**, 184303 (2012).

[90] A. A. El-Sharkawy, A. M. A. El-Azm, M. I. Kenawy, A. S. Hillal, and H. M. Abu-Basha, Thermophysical properties of polycrystalline PbS, PbSe, and PbTe in the temperature range $300 - 700$ K, Int. J. Thermophys. **4**, 261 (1983).

[91] L. Lindsay, D. A. Broido, and N. Mingo, Flexural phonons and thermal transport in graphene, Phys. Rev. B **82**, 115427 (2010).

[92] T. Feng and X. Ruan, Four-phonon scattering reduces intrinsic thermal conductivity of graphene and the contributions from flexural phonons, Phys. Rev. B **97**, 045202 (2018).

[93] M. B. Smith, K. Page, T. Siegrist, P. L. Redmond, E. C. Walter, R. Seshadri, L. E. Brus, and M. L. Steigerwald, Crystal structure and the paraelectric-to-ferroelectric phase transition of nanoscale $BaTiO_3$, J. Am. Chem. Soc. **130**, 6955 (2008).

[94] Y. Xia and M. K. Y. Chan, Anharmonic stabilization and lattice heat transport in rocksalt β-GeTe, Appl. Phys. Lett. **113**, 193902 (2018).

[95] V. V. Goldman, G. K. Horton, and M. L. Klein, An Improved Self-Consistent Phonon Approximation, Phys. Rev. Lett. **21**, 1527 (1968).

[96] Y. Oba, T. Tadano, R. Akashi, and S. Tsuneyuki, First-principles study of phonon anharmonicity and negative thermal expansion in ScF_3, Phys. Rev. Mater. **3**, 033601 (2019).